Contents

Chapter 1

Introduction

The end of the 19th century and the 20th century were rich in new discoveries in the field which today is called *"nuclear physics"* [1]. In 1896 H. Becquerel discovered radioactivity in uranium, a fact which proved that the atomic nucleus can change its form and emit energy. Radioactivity became an important tool for revealing the interior of the atom. In 1898 the French physicists P. Curie and M. Curie discovered the radioactive elements polonium and radium, which occur naturally in uranium minerals. In 1911 E. Rutherford made his greatest contribution to science and showed that the positive charge in the atom is concentrated in a very small central nucleus some 10000 times smaller in diameter than that of the atom. In 1920, based on earlier studies of W. Wien (1898) and J. J. Thomson (1910) who identified a positive particle equal in mass to the hydrogen atom, Rutherford accepted the hydrogen nucleus as an elementary particle, called proton. Twelve years later, in 1932, J. Chadwick discovered the neutron. Parallel with this discovery, the first cyclotron was built in 1932 by E. O. Lawrence. This device accelerated hydrogen ions (protons) to an energy of 13000 electron volts (eV). In 1935 I. Joliot-Curie and F. Joliot made the first artificial radioactive isotope by bombarding ^{27}Al with α-particles, which constituted an important step towards the solution of the problem of releasing energy by the nucleus. Inspired by this work, in 1936 E. Fermi produced artificial radioactive isotopes by using neutrons. In 1939 L. Meitner reported that the uranium atom had been split into two parts after the bombardment with slow neutrons. The new phenomenon was called fission. Already in 1937 N. Bohr and F. Kalckar proposed that nuclei can possess a collective rotation as motion. The collective model and its relation to the single-particle motion was then developed by A. Bohr, B. Mottelson, and J. Rainwater in the early 1950s. In 1955 M. Goeppert Mayer and J. H. D. Jensen proposed the shell model, which describes the structure of some atomic nuclei, and in 1962 S. M. Poliakov discovered fission isomers the first superdeformed nuclei. Also in 1962 the first γ-ray spectrum using a Ge(Li) detector was obtained.

Since then, great progress has been made in the understanding of the nucleus both from experimental and theoretical point of view, and the advent of the latest generation of 4π Germanium detector arrays such as Gammasphere and Euroball has allowed for more detailed and refined studies.

High-spin states in $N \approx Z$ nuclei in the mass $A \sim 60$ region have been studied in a series of experiments involving these "Big Arrays", which were combined with dedicated charged-particle detector arrays. The experiments have established well and superdeformed bands in some Ni, Cu, and Zn isotopes and established a new island of superdeformation around particle numbers $N, Z \approx 28 - 30$. Moreover, some of these bands in the second well of the nuclear potential were found to decay by prompt particle emission towards spherical states in the corresponding daughter nucleus, in competition to the expected γ-ray decay towards the normally deformed states in the first minimum of the same nucleus. Comparative studies of the observed highly deformed band in ^{59}Cu and the superdeformed bands in ^{58}Cu and ^{60,61}Zn have already been performed with different theoretical calculations. On the other hand, the decay-out process of these bands have just started to be investigated and compared with similar decay-out processes in heavier mass regions, and the theory of prompt proton decay is still in progress.

This thesis is about experimental nuclear structure studies in the mass $A \sim 60$ region, and focuses on the $N = Z + 1$ nucleus ^{59}Cu. It is based on the following publications:

- **Yrast Superdeformed Band in ^{59}Cu**[1]
  C. Andreoiu, D. Rudolph, C.E. Svensson, A.V. Afanasjev, J. Dobaczewski, I. Ragnarsson, C. Baktash, J. Eberth, C. Fahlander, D.S. Haslip, D.R. LaFosse, S.D. Paul, D.G. Sarantites, H.G. Thomas, J.C. Waddington, W. Weintraub, J.N. Wilson, and C.-H. Yu.

  Phys. Rev. C**62**, 051301(R) (2000).

- **Prompt Proton Decays in ^{58,59}Cu**
  C. Andreoiu, D. Rudolph, C. Fahlander, A. Gadea, D.G. Sarantites, C.E. Svensson, and the GSFMA66 and EB98.02 collaborations.

  Proceedings *Pingst2000 - Selected Topics on $N = Z$ Nuclei*, June 2000, Lund, Sweden, Eds. D. Rudolph and M. Hellström, KFS AB Lund, to be published.

[1]Paper I is reprinted with the permission of the copyright holder. Copyright 2000 by The American Physical Society.

Chapter 2

General Aspects

2.1 Superdeformation

In the shell model description of nuclei it is suggested that the nucleons move in specific orbits with specific energy and angular momentum in a similar way as the electrons in the atom. The orbits form a shell structure, and two orbits are occasionally separated by large energy gaps. A certain number of protons and neutrons fills a major shell corresponding to the "magic" numbers for protons and neutrons (Z, N = 2, 8, 20, 28, 50, 82, 126, and 184). These nuclei are called "magic nuclei". They are more stable than others, which e.g. means that more energy is needed to separate one of the nucleons from such a nucleus as compared to one of its neighbours. The magic nuclei have a spherical shape.

By adding more valence nucleons above a shell closure, nuclei start to become deformed. Historically, the concept of nuclear shape appeared first in the description of the nuclei in the framework of the liquid drop model. The nucleus is described as a liquid drop, and it may present dynamic deformation through surface and volume vibrations around a spherical equilibrium shape, or it may have a static deformation in which it can rotate very fast. A typical deformed nucleus in the rare-earth region has prolate shape (lemon shape) with a quadrupole deformation of $\beta_2 \approx 0.2$.

The Nilsson scheme presented in Fig. 2.1 shows the single-particle energies of the neutron orbits versus the quadrupole deformation for nuclei in the mass $A \sim 60$ region [2]. For spherical magic nuclei, i.e., at no deformation, one can see that the energy gaps at neutron numbers 20, 28, and 40 are large. At a quadrupole deformation of $\beta_2 \approx 0.2$ the gaps disappear. The Nilsson diagram for single-particle energies of a deformed nucleus is very different from that of a spherical nucleus. Moving towards a larger deformation of $\beta_2 \approx 0.4$ a new distinct energy gap is formed corresponding to 28 neutrons [3]. This corresponds to the spherical nucleus $N = Z = 28$ ^{56}Ni, which thus is doubly-magic both at spherical and deformed shape. At an even larger deformation of $\beta_2 \approx 0.5$ another gap is formed at neutron number 30. This is the superdeformed "doubly-magic" core for the $N = Z = 30$ system, i.e., for ^{60}Zn [4].

Superdeformation corresponds to an elongated shape with a major-to-minor axis ratio of 2:1. The existence of superdeformed shapes in nuclei was evidenced for

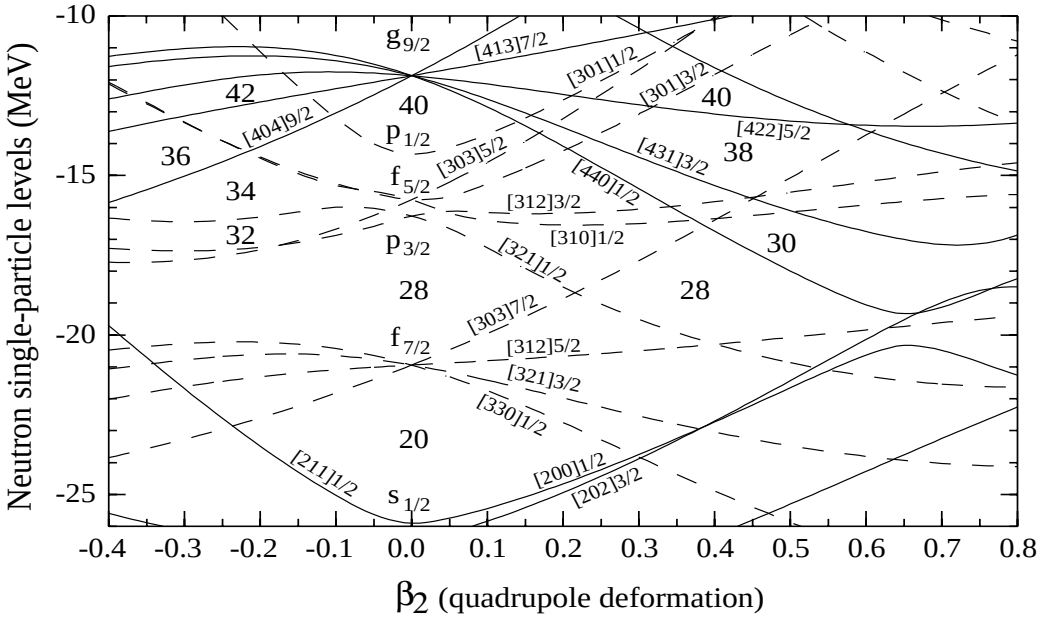

Figure 2.1: The neutron single-particle levels for the mass $A \sim 60$ region from calculation using a Wood-Saxon potential versus quadrupole deformation, β_2 [2].

the first time in the actinide fission isomers [5], and it was theoretically explained through the existence of a second minimum of the nuclear potential at very large deformations [6]. The first and the second minima of the nuclear potential, separated by an energy barrier, are schematically illustrated in Fig. 2.2, which shows the potential energy of a nucleus versus deformation. The states in the second minimum correspond to very elongated or superdeformed shapes, which in the actinides region were found to decay either by spontaneous fission or by γ-rays back into the first well of the potential.

The experimental evidence for a superdeformed nucleus at high spin is the emission of very fast rotational γ-ray transitions with regular energy spacing. Until today more than 200 superdeformed rotational bands have been observed in different mass regions of the nuclidic chart, ranging from $A \sim 190$ nuclei down to the $A \sim 30$ region. The first high-spin superdeformed band was discovered in ^{152}Dy in 1986 [7] in the mass $A \sim 150$ region and it was followed in 1989 by the discovery of a superdeformed band in the mass $A \sim 190$ region in the ^{192}Hg nucleus [8]. In the mass $A \sim 130$ region the first superdeformed band was observed in ^{132}Ce [9]. The first superdeformed band in the medium-mass $A \sim 80$ region was observed in the ^{83}Sr nucleus [10]. In the mass $A \sim 60$ region the first superdeformed band was found in ^{62}Zn [11]. Recently, a superdeformed band was reported in the $A \sim 30$ region, namely in ^{36}Ar [12].

In Fig. 2.3 the dynamical moments of inertia, $J^{(2)}$ (see Chapter 5.2 for definition), are plotted as a function of the rotational frequency for a few superdeformed bands from different regions of superdeformation. In order to remove its mass dependence $J^{(2)}$ was divided by $A^{5/3}$. Evidently, the rotational frequency increases as the mass decreases, and the dynamical moments of inertia vary within a narrow range. Their

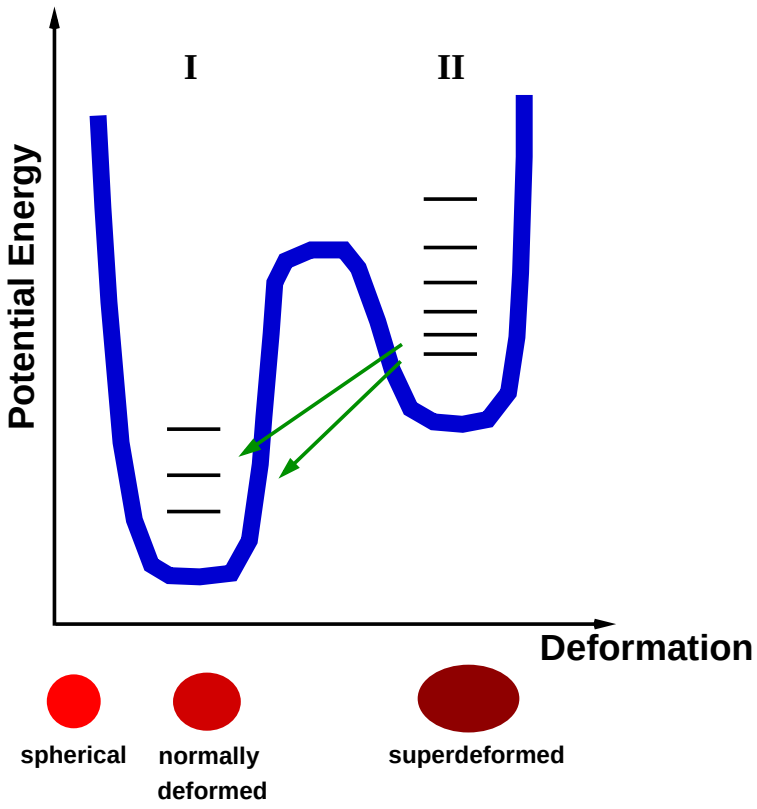

Figure 2.2: The potential energy of a nucleus versus the deformation.

values approximately equal the moment of inertia of a rigid body of axial symmetric deformation $\beta_2 = 0.5$ (dashed line).

The nucleus dramatically changes its shape when it decays from the superdeformed states towards the normally deformed states. The transitions connecting the states in the second minimum with the states in the first minimum of the potential (see Fig. 2.2) are called the linking transitions. They define the superdeformed band in terms of excitation energy, spin, and parity, and give important information about the decay-out mechanism of these bands. The linking transitions are very hard to observe due to their low intensity. There are important peculiarities between the linking transitions in the mass $A \sim 60$ region with respect to heavier mass regions. For example, in the mass $A \sim 190$ the level density of the states in the first minimum of the potential is high, the nucleus has more possibilities to decay, and the superdeformed states may be more strongly mixed with highly excited normal states. In this case one may expect that the decay-out process is statistical. Usually, these linking transitions are stretched $E1$, which means that they change the parity of the states, and the spin difference of the states is equal to one unit of angular momentum. On the contrary, in the $N = Z$ nucleus ^{60}Zn the level density of the states in the first minimum is relatively small, the transitions from the superdeformed states to the normally deformed states take place with no change in parity, and the spin difference is two units of angular momentum. It is suggested that the decay-out process may be non-statistical [4].

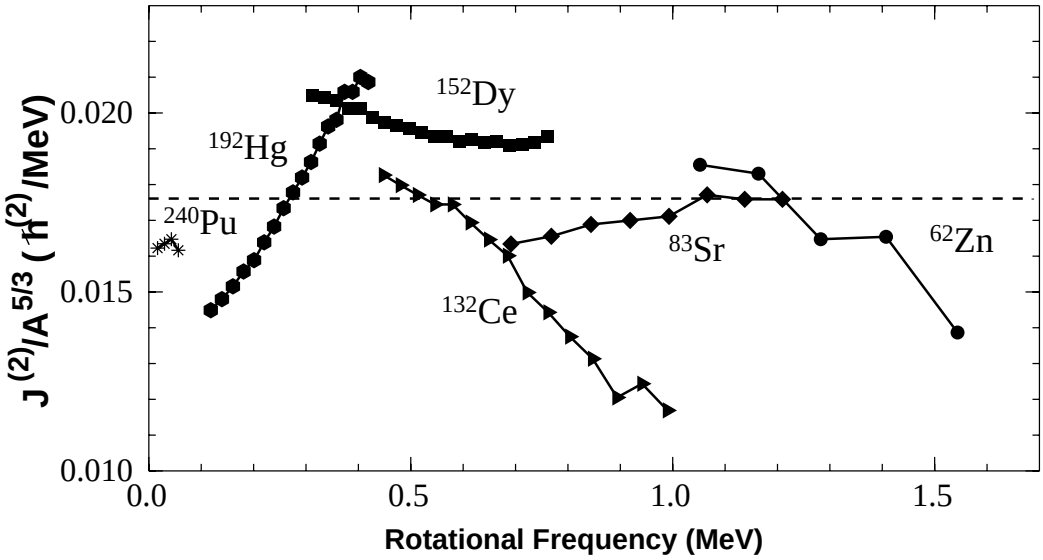

Figure 2.3: Dynamic moment of inertia $J^{(2)}$ divided by $A^{5/3}$ versus rotational frequency for superdeformed bands from different mass regions. The dashed line represents the moment of inertia of a rigid rotor with quadrupole deformation $\beta_2 = 0.5$. Taken from Ref. [11].

Figure 2.4 shows the nuclidic chart for the mass $A \sim 60$ region, which is the main focus of this thesis. The number of neutrons and the number of protons are given on the x and y axis, respectively. The $N = Z$ nuclei having the same number of neutrons and protons are indicated by the grey squares. Also the names of the elements lie beside their chain of isotopes. The numbers in each square indicate the number of nucleons of the isotope, and below it the populating reaction channel for each isotope observed in one of the performed experiments (GS90) is shown. The filled circles stand for published well- or superdeformed bands, while the unfilled circles stand for known but unpublished well- or superdeformed bands. In this mass region, a superdeformed band was first observed in the ^{62}Zn nucleus [11]. It was followed by the observation of superdeformed bands in the $N = Z$ nuclei ^{56}Ni [13], ^{58}Cu [14], and ^{60}Zn [4], and in the $N = Z + 1$ nuclei ^{61}Zn [15] and ^{59}Cu. The superdeformed band in ^{60}Zn represents the $N = Z = 30$ "doubly-magic" superdeformed core of the $A \sim 60$ mass region [4].

These superdeformed bands belong to nuclei in the (until recently) lightest mass region where superdeformation has been observed. They are very interesting because they are the fastest rotating nuclei known ($\hbar\omega \approx 1.5 - 2$ MeV) and because they are self-conjugate ($N = Z$) or nearly self-conjugate ($N \approx Z$), which means that aspects such as isospin $T = 0$ pairing correlations might be important for their description. Although most of the superdeformed bands in this region were linked to the normally deformed states, only in the ^{60}Zn and ^{59}Cu nuclei the superdeformed band have the spins and parities firmly assigned.

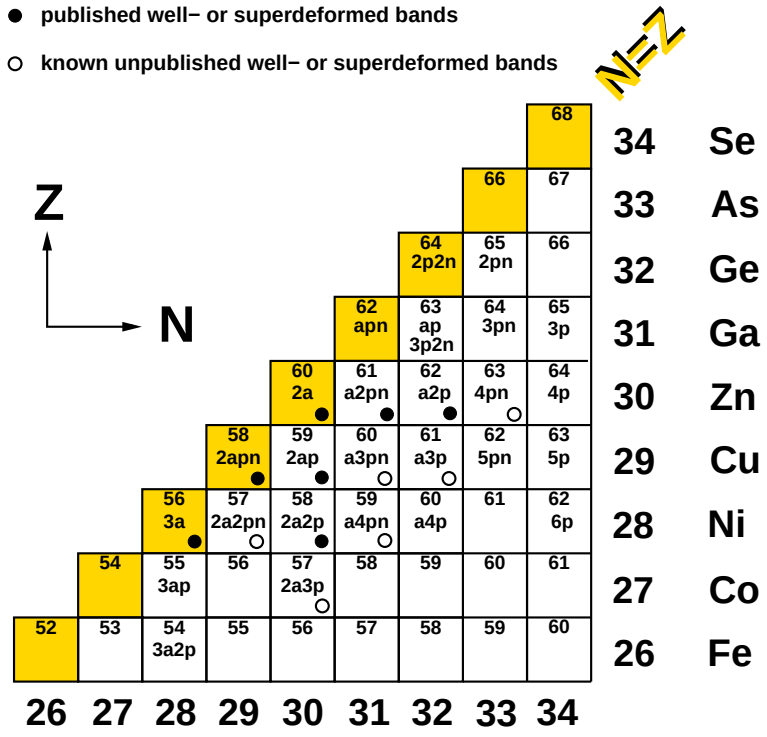

Figure 2.4: The nuclidic chart around the mass $A \sim 60$ region.

2.2 Prompt Proton Decays

Proton radioactivity and β-delayed proton decay are two well-known types of proton decays, which have been observed for the first time in 1970 and 1976, respectively. One example of proton radioactivity from an excited state in the parent nucleus [16] is shown in the right panel of Fig. 2.5 [17]. The $I^{\pi} = 19/2^{-}$ state in ^{53}Co has a long lifetime (247 ms). It is called an isomeric state. The β^{+} decay from this isomeric state to the daughter nucleus ^{53}Fe is competing with proton decay into the daughter nucleus ^{52}Fe, which is a very weak branch ($\approx 1.5\%$). The proton energy is $E_{p,c.m.} = 1.56$ MeV. The experiments which evidenced these types of proton radioactivity are based on discrete-line spectroscopy. The first evidence for proton radioactivity from a ground state was discovered in 1981 for the ^{151}Lu nucleus into the daughter nucleus ^{150}Yb [18].

The process of β-delayed proton emission [19] is illustrated in the left panel of Fig. 2.5. The proton rich ^{53}Ni nucleus decays into states of high excitation energy and high level density of the daughter nucleus ^{53}Co. These low-spin states decay either via γ-ray towards the ground state of ^{53}Co, or by fast proton emission (usually with angular momentum $l = 0$) towards the ground state of ^{52}Fe. This process is possible because the Q-window for the β^{+} decay is large (13.2 MeV) and the proton binding energy of ^{53}Co is small (1.6 MeV). The β-delayed proton emission spectrum is quasi-continuous.

A new type of proton decay, so-called **prompt proton decay**, was observed for

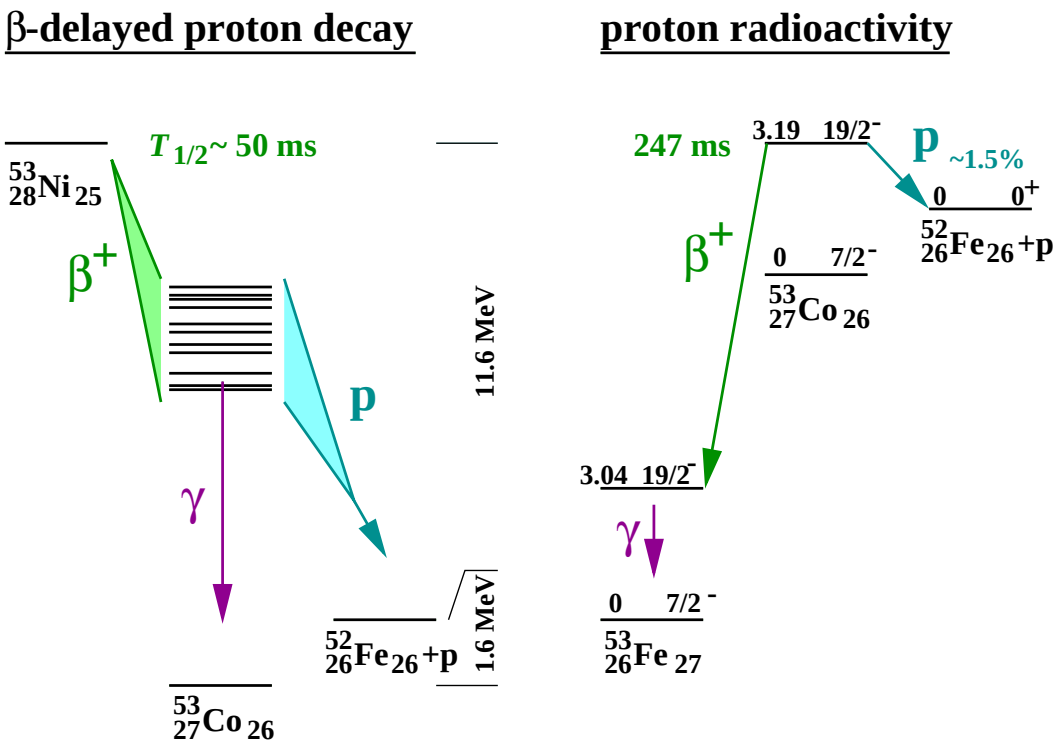

Figure 2.5: Two different types of proton decay previously observed in low-energy nuclear structure studies: β-delayed proton decay from highly excited low-spin states (left) and the proton radioactivity (right). Taken from Ref. [17].

the first time in ^{58}Cu [14]. It is shown in Fig. 2.6, where also the states in the first minimum of the potential and the rotational band in the second minimum of the potential are illustrated. The band head in the second minimum has most likely spin and parity $I^{\pi} = (9^{+})$, and the band is assigned a configuration involving one proton and one neutron in the $g_{9/2}$ orbital $[\pi(g_{9/2}) \otimes \nu(g_{9/2})]$. This band decays by both γ-ray transitions towards the spherical states in ^{58}Cu and by prompt ($\tau < 1$ ps) proton emission towards the spherical states in the daughter nucleus ^{57}Ni. A second case of prompt proton decay was later established in the decay-out of a rotational band in ^{56}Ni into the ground state of ^{55}Co [13], and recently two prompt proton decays from deformed states in ^{59}Cu were observed, which are the subject of the present thesis. Moreover, there is experimental evidence for a prompt discrete α decay from the deformed band in the second potential well of ^{58}Ni into the spherical 6^{+} yrast daughter state in ^{54}Fe [20].

There are major differences between the 'conventional' proton emission processes and these prompt proton decays [17]:

- The prompt particle decays compete with γ-radiation, while the (ground or isomeric state) proton radioactivity competes with β^{+} decay.

- The prompt proton decays carry an angular momentum of $l \sim 4\hbar$, while β-delayed protons are represented by s or p-waves ($l \sim 0\hbar$ or $l \sim 1\hbar$).

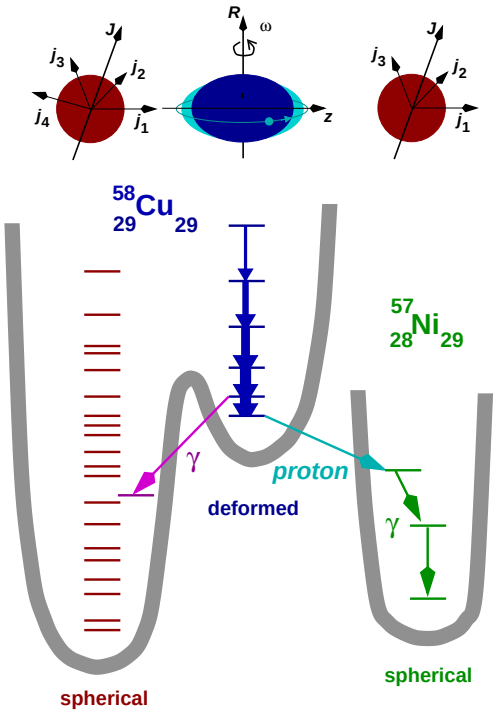

Figure 2.6: Schematic picture of the prompt proton decay in ^{58}Cu from the deformed band in the second minimum of the potential into the spherical daughter state in ^{57}Ni. Taken from Ref. [13]

- The time scale is different by several orders of magnitude. Proton emitters possess typical half-lives in the micro- to millisecond range. β-delayed protons are *observable* on a similar time scale but, the proton decay times are much faster, i.e., in the attosecond regime (10^{-18} s). The prompt particle decays, however, seem to lie in the picosecond range (10^{-12} s).

- There is a drastic change of nuclear shape involved in the prompt particle decays. The initial states, situated at the bottom of the rotational bands, have a deformation of $\beta_2 \sim 0.4$, while the final states are spherical shell-model states. For the conventional proton decays, the shapes associated with the initial and final nuclear states are essentially the same.

Chapter 3

Experimental Methods

3.1 The Compound Nucleus Reaction

The excited states of a nucleus can be populated in many ways according to the purpose of the study. One of the most useful techniques to reach high-spin states is by populating the nucleus of interest through the compound nucleus mechanism. Figure 3.1 shows a schematic drawing of this process, which was suggested by N. Bohr and F. Kalckar already in 1937 [21].

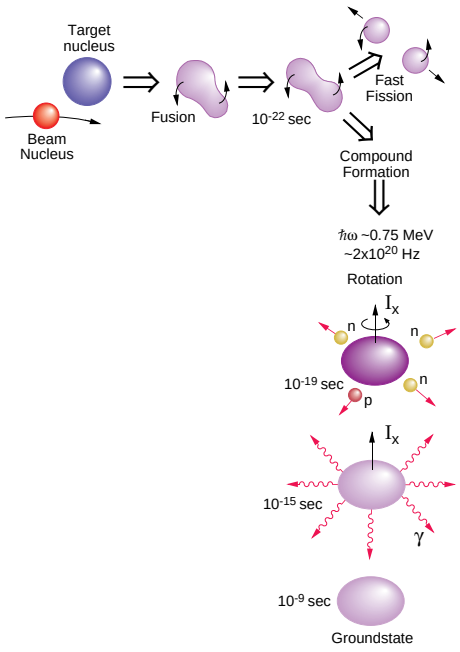

Figure 3.1: Time evolution for compound nucleus formation and decay. Taken from Ref. [22].

The beam consists of nuclei which are accelerated to energies of about 3-5 MeV per nucleon. The projectile bombards a target foil, which is made of enriched material of a specific isotope. The two nuclei fuse and form a compound system. The

system, which has a lot of excess energy, cools down by evaporating light particles such as protons, neutrons, and α-particles leading to different residual nuclei. The time scale for this process is of the order of 10^{-19} s. The residual nucleus is left in a state at high excitation energy and high angular momentum and first decays via statistical γ-decay towards the yrast line. The yrast line is defined as the state of lowest energy for a given angular momentum. Close to the yrast line the level density is low enough to enable observation of emitted discrete γ-ray transitions of the nucleus towards the ground state. The nucleus reaches its ground state in about 10^{-9} s. These discrete γ-rays are resolved in the experiment and give information about the nucleus of interest, which is to be studied.

3.2 Gamma Ray Detection; Gammasphere

Figure 3.2: Ge detectors from the Gammasphere array. Taken from Ref. [22].

The main tools for nuclear γ-ray spectroscopy are germanium (Ge) detectors. Germanium is a semiconductor material which has a good energy resolution in detecting γ-rays, due to the small ionization energy necessary to excite an electron from the valence band into the conduction band. The γ-rays are more efficiently detected by high-Z materials because the photoelectric cross section is proportional

to Z^5. For typical Ge detector, which has a cylindrical shape, with diameter and length of about 7-9 cm an incident γ-ray with an energy of 1 MeV produces a full-energy peak with a resolution of about 2 keV. The detection efficiency of a single germanium detector is rather limited by its size and it is generally compared to the efficiency of a 7.62×7.62 cm NaI(Tl) detector.

The interaction of γ radiation with matter is described by three basic effects: the photoelectric absorption, Compton scattering, and pair production. In the photoelectric absorption the γ-ray energy is completely absorbed in the germanium detector. In the Compton process the γ-ray transfers only a part of its energy to the electrons in the crystal and part of the γ-ray energy may escape from the detector. This results in a large, continuous background, which can be suppressed by surrounding the Ge crystal with BGO[1] Compton-suppression shields (see Fig. 3.2). The peak-to-total ratio is improved by rejecting the γ-rays, which are Compton scattered out of the Ge crystal. Normally Heavimet collimators are placed in front of the BGO detectors in order to decrease false vetoes in high-multiplicity events and to increase the peak-to-total ratio at low energies. If the Heavimet collimators are removed from the BGO detectors the experiment can provide event-by-event γ-ray sum-energy [23], multiplicity measurements, and additional channel selectivity by total energy conservation requirements [24] (see also Chapter 4.1).

A common problem for heavy-ion experiments is the loss of energy resolution of the γ-ray lines due to Doppler broadening. The γ-rays emitted in flight from a residual nucleus produced in a heavy-ion reaction have an appreciable Doppler shift. The Doppler-shifted energy, E_γ, is related to the unshifted energy E_0 by the following relation

$$E_\gamma = E_0(1 + \frac{v}{c}cos\theta) \tag{3.1}$$

where θ is the angle of the emitted γ-ray with respect to the recoil nucleus direction. It is assumed that the recoiling nucleus velocity v in the laboratory frame is small compared to the velocity of light c. For the thin target experiments the major contribution to Doppler broadening of the spectrum peaks comes from the finite opening angle of the detector array. Since the Doppler shifted γ-ray energy depends on θ, the dependence of the broadening, ΔE_γ is obtained by the partial derivative of (3.1)

$$\Delta E_\gamma = E_0 \frac{v}{c} sin\theta \Delta\theta \tag{3.2}$$

where $\Delta\theta$ is the opening angle of the detector as seen from the target. According to Eq. (3.2) the Doppler broadening is maximum for $\theta = 90°$. This effect can be partially corrected for by segmenting the Ge detectors into two or more parts, thus reducing the opening angle of the detector. Another significant contribution to the Doppler broadening comes from the velocity variation of the recoiling nuclei due to energy-loss straggling in the target. It means that the recoiling nuclei have different velocity vectors due to interaction with the target material. According to Eq. (3.1) this effect depends on cosθ, and it is maximum for the detectors sitting at 0° and 180°. To correct this effect it is assumed that the reaction takes place

[1] $Bi_4Ge_3O_{12}$

in the middle of the target with an effective beam energy. In this approximation the energy and velocity of the compound nucleus can be determined. The third significant contribution to the Doppler broadening is due to the emission of the evaporated particles (see also Chapter 3.3).

The granularity of a multidetector system refers to the possibility to localize individual γ-rays and its ability to reduce the probability that two γ-rays hit one detector in the same event. In heavy-ion reactions, which often give rise to high γ-ray multiplicity events, a high granularity of the detector setup helps to distinguish double hits. To obtain both a high resolution, a high granularity, and a high efficiency it is thus necessary to combine many Ge detectors into a large γ-ray array.

Gammasphere [25] is one such big γ-ray detector array. It is presently situated at the Lawrence Berkeley National Laboratory in U.S.A. The complete geometry of Gammasphere consists of 110 Ge detectors placed in a spherical shell, each of them being enclosed in a BGO Compton-suppression shield (see Fig. 3.2). A large number of detectors is two-fold segmented. Gammasphere has a full-energy peak efficiency of about 9% at a γ-ray energy of 1.3 MeV, and a full width at half maximum better than 2.6 keV at the same energy.

Euroball [26] is the European γ-ray array spectrometer, presently situated at "L' Institut de Recherches Subatomiques Strasbourg" (IReS), France. It consists of 239 germanium detectors grouped in 15 cluster detectors, 26 clover detectors, and 30 individual germanium detectors. A cluster detector consists of seven individually encapsulated germanium detectors. Each of these detectors has an efficiency of about 60% relative to a 7.62×7.62 cm NaI(Tl) detector at a γ-ray energy of 1.33 MeV. Each clover detector contains four separate germanium crystals packed together in a four-leaf clover arrangement. The energy resolution of each crystal is about 2.1 keV at 1.33 MeV. The photopeak efficiency for each crystal is about 21% relative to a 7.62×7.62 cm NaI(Tl) detector. The relative efficiency of the individual germanium detectors is about 65-80%. Each of these types of detectors is surrounded by a BGO anti-Compton shield in order to take care of the Compton scattering effect. The clover and cluster detectors have the property that the energies of the Compton scattered γ-rays registered in neighbouring crystals can be recovered to total absorption events. When the energy of a γ-ray is deposited in two neighbouring Ge detectors, then the energies can be summed up, so that the energy in a large number of events can be determined. Thus the efficiency of the composite detector approaches that of an individual crystal with the same volume. As a result the Compton background is reduced, the peak to total ratio is enhanced, and the photopeak efficiency is increased. The Euroball array is structured as follows: the 30 individual germanium detectors are sitting at forward laboratory angles, the clover detectors are placed in two rings in the central section, and the cluster detectors are situated at backward angles.

3.3 Proton and Alpha Detection; Microball.

The compound nuclei produced on the proton rich side of stability tend to decay back towards the valley of the line of stability by emitting protons and α-particles rather than neutrons, since the Coulomb barrier for these nuclei is lower than normal and the binding energy of neutrons is large. In heavy-ion induced fusion-evaporation reactions far from stability a large number of exit channels are populated. Some of them have very small cross sections. One of the most important tasks is to select a specific channel by gating on the evaporated particles. For this purpose, ancillary detectors are used to measure light evaporated particles in coincidence with γ-rays.

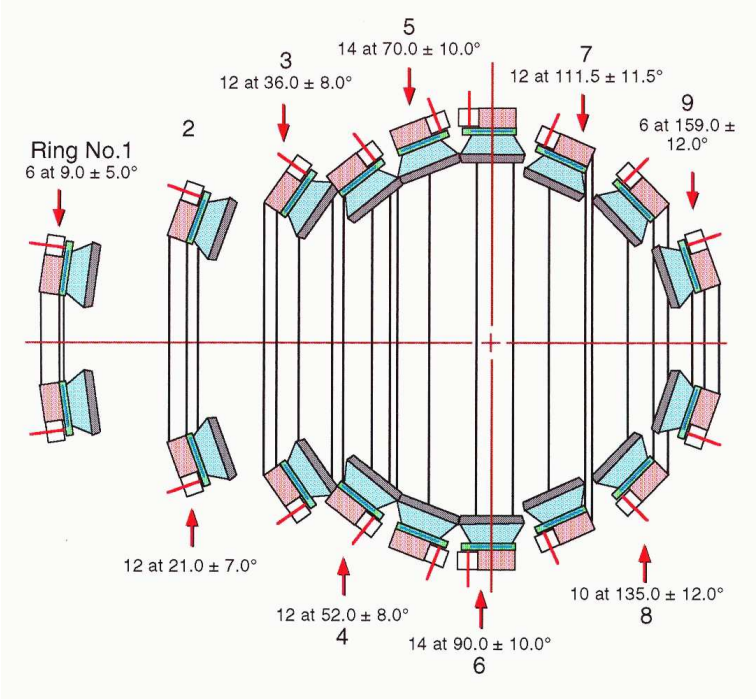

Figure 3.3: Schematic drawing of the 4π CsI array Microball. Taken from Ref. [27].

Microball [27] is such an ancillary detector which detects light charged particles emitted from the reaction process. It consists of 95 CsI(Tl) elements placed in 9 rings (see Fig. 3.3) in a 4π geometry, and it was designed to fit inside the Gammasphere array. The 9 rings of detectors cover the angles between 4.0° and 171° relative to the beam. Due to the motion of the recoiling nuclei, the emitted particle will be registered mostly in the forward direction in the laboratory frame. Therefore, in order to increase the granularity of the Microball array, the two most forward rings of detectors were placed at larger distances from the target.

Protons and α-particles are discriminated in Microball by pulse shape techniques [27]. From each Microball element three signals are of interest: time, energy, and charge ratio. The charge ratio is a parameter which is determined by the fact that the scintillations produced in the CsI(Tl) material have two decay components. The

first one has a time response less than 1μs (fast component) and its shape depends on the particle type detected. The second component has a time response of 7μs (slow component) and its shape is independent of particle type detected. These two components determine the charge ratio between the early and late part of the pulse which is thus used to distinguish between particle types. The front surface of each detector is covered by absorbers to stop the elastically scattered heavy-ion beams which otherwise would damage the CsI(Tl) detectors.

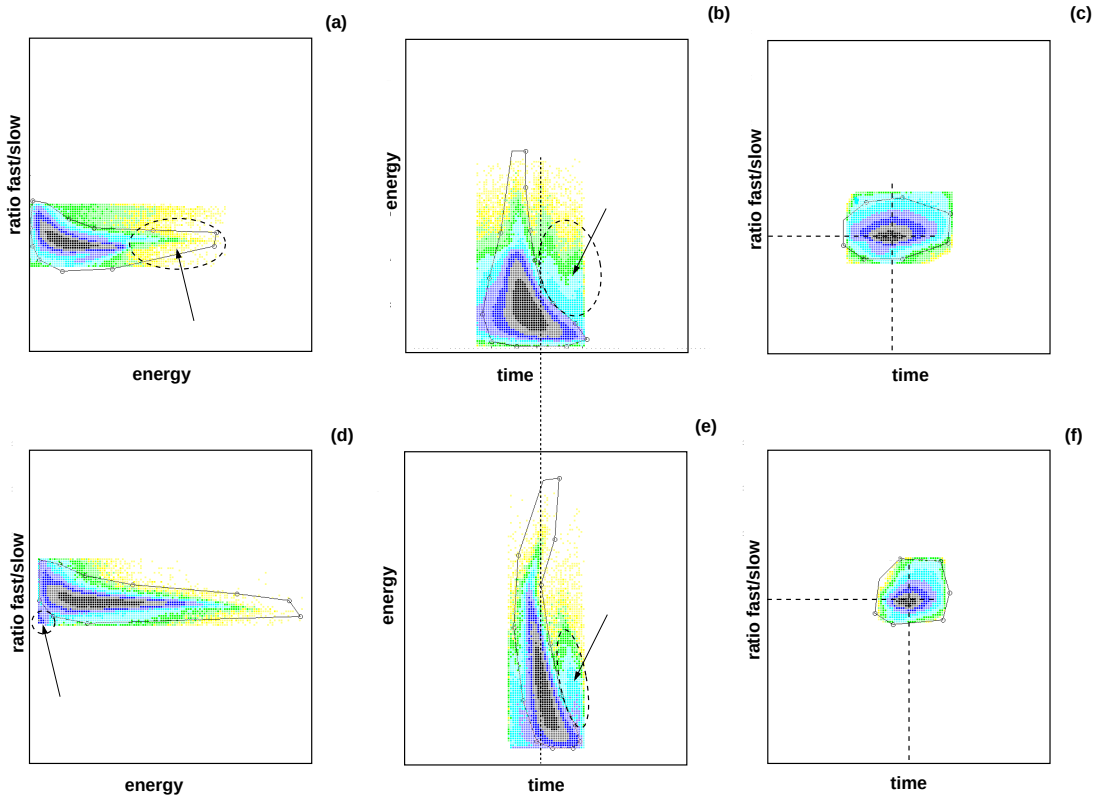

Figure 3.4: Two-dimensional spectra from the Microball detector element 29 situated in the fourth ring. The three combinations of signals from Microball determine the particle identification. See text for details.

Figure 3.4 shows six two-dimensional spectra from the 29-th element of Microball situated in the fourth ring. The proton spectra are shown in the first row and the α-particle spectra in the second row. We impose a triple two-dimensional gating procedure. The spectra (c) and (f) in Fig. 3.4 are already gated by the two two-dimensional gates set in the matrices 'energy vs. ratio' and 'energy vs. time'. The spectra (a) and (d), and (b) and (e) are correspondingly gated by the other two two-dimensional gates. This is done in an iterative fashion until a clear separation (Fig. 3.4) is obtained. The solid-line closed contours are the final gates for protons and α-particles used in the analysis. In panel (c) and (f) one clearly sees the difference in charge ratio for protons and α-particles. This fact provides a good separation between the two types of particles and represents the first step in the

particle discrimination procedure. In panel (a) the solid-line contour encloses the selected protons, and in the dashed elliptical contour are either two-proton pile-up or deuteron events. The solid-line contour in panel (a) eliminates the electronic noise or remaining ambiguities left from the two other gates. In panel (d) the α-particles selected in the solid-line contour reach higher energies than the protons. The dashed circle and the arrow outside the solid-line contour indicate electrons and/or leaking protons which are eliminated. The panels (b) and (e) give indication about the protons and α particles detection time. The events from the next beam pulse lie in the dashed elliptic contour.

The Microball detector determines the energies and angles, and hence the momenta of the emitted charged particles event-by-event. The momentum of the recoiling nucleus can then be found and thus the angle between the recoiling nucleus and each Ge detector can be determined. This is used for "kinematic correction" of the γ-rays emitted in flight, which allows for a more precise determination of the γ-ray energies. The calibration of the Microball detector is typically done using a beam of protons and α-particles with energies of 12 and 48 MeV. The beams are elastically scattered on ^{197}Au and inelastically scattered on ^{12}C and the produced peaks are used for calibration. For the backward detectors the calibration is done with an α source with 6.051 and 8.785 MeV lines.

3.4 Neutron Detection; Neutron Wall.

In a fusion-evaporation experiment the compound nucleus can emit also neutrons. Evaporated neutrons are preferentially emitted in the forward direction due to the kinematic focusing. They barely interact with high-Z materials. Therefore, they are detected in big liquid scintillator detectors. In conjunction with Gammasphere 15 liquid scintillator neutron detectors were used in two of the below presented experiments, replacing the Ge-detectors located in the three most forward rings. This array can provide information about the number of the emitted neutrons to identify γ-ray transitions belonging to a specific nucleus.

3.5 Experiments

High-spin states in the residual nucleus ^{59}Cu were populated in three experiments performed at Lawrence Berkeley National Laboratory (GS54 and GS90) and at Argonne National Laboratory (GSFMA66), U.S.A. The first two experiments were the source of information for the observation of the yrast superdeformed band in ^{59}Cu, and the third experiment revealed the prompt proton decays from the rotational superdeformed bands. The main characteristics of the experiments are summarized in Table 1, but there are some details which should be mentioned.

In the GS54 experiment the target consisted of a 0.42 mg/cm^2 layer of ^{28}Si, which was evaporated onto a 0.9 mg/cm^2 Ta foil. The Ta foil faced the beam, thus reducing the energy to 136 MeV. In this reaction the compound nucleus was ^{64}Ge, and ^{59}Cu was populated in the 1α1p channel. The event trigger required the

GS54	GS90	GSFMA66
^{36}Ar + ^{28}Si E_{beam} = 143 MeV Target ^{28}Si: 0.42 mg/cm^2 CN: ^{64}Ge Channel: 1α 1p Gammasphere (82 Ge) Microball + 15 neutron detectors σ_{rel} =3% Trigger: 1n2γ ,$\gamma\gamma\gamma$	^{28}Si + ^{40}Ca E_{beam} = 125 MeV Target ^{40}Ca : 0.5 mg/cm^2 CN: ^{68}Se Channel: 2α 1p Gammasphere (82 Ge) Microball + 15 neutron detectors σ_{rel} =5% Trigger: 1n2γ ,$\gamma\gamma\gamma$	^{28}Si + ^{40}Ca E_{beam} = 122 MeV Target ^{40}Ca: 0.5 mg/cm^2 CN: ^{68}Se Channel: 2α 1p Gammasphere (103 Ge) Microball σ_{rel} ~6% Trigger:$\gamma\gamma\gamma\gamma$

Table 1. Characteristics of the experiments performed to study ^{59}Cu.

detection of either three γ-rays or two γ-rays and one neutron. A total of 2×10^9 events were collected.

So far, the major source for the analysis of the level scheme of ^{59}Cu has been GS90. The total cross section for the ^{28}Si + ^{40}Ca reaction at a beam energy of 125 MeV is $\sigma \approx 1$ b. The relative experimental cross section for ^{59}Cu (in this reaction populated in the 2α1p channel) is $\sigma_{rel} \approx 5\%$ and for ^{58}Ni is $\sigma_{rel} \approx 9\%$. The trigger event required coincidences between at least two Ge detectors and one neutron detector or between three Ge detectors and 2.7×10^9 events were recorded. Due to the smaller number of evaporated α-particles the GS54 experiment populated the ^{59}Cu nucleus at higher excitation energies and angular momenta than the GS90 experiment. The 1α1p channel corresponding to ^{59}Cu in the GS54 experiment had a higher degree of contamination from the 1α2p channel corresponding to ^{58}Ni in comparison with the GS90 experiment. Therefore, the GS90 experiment was more favorable than the GS54 experiment to analyze ^{59}Cu. Both GS54 and GS90 had neutron detectors in the experimental set-up. However, the channels corresponding to ^{59}Cu did not involve neutron evaporation. Therefore, the neutron detectors were not used in the data analysis.

The GSFMA66 experimental set-up did not involve neutron detectors. Therefore, the number of Ge detectors was higher. It used the same reaction as in the GS90 experiment but the beam energy was smaller, which means that the low-spin states were more populated. It also led to a smaller cross section for ^{58}Ni, which is the major source of contamination for ^{59}Cu. The GSFMA66 experiment provided 8 times more statistics than the GS90 experiment and the event trigger required at least four γ-rays being detected. In the GS90 and GSFMA66 experiments the Heavimet collimators were removed from the Gammasphere detectors to provide event-by-event γ-ray sum-energy [23], multiplicity measurements, and additional channel selectivity by total energy conservation requirements [24]. Following GSFMA66, the energy and efficiency calibration of the Gammasphere detectors were done using ^{56}Co, ^{60}Co, ^{88}Y, ^{152}Eu, ^{113}Sn, ^{137}Cs, and ^{228}Th γ-ray sources. This extensive calibration gives the response function of Gammasphere including the Microball detector.

Two more experiments were performed to explore nuclei in the mass $A \sim 60$ region. They are summarized in Table 2.

Euroball	GSFMA42
^{24}Mg + ^{40}Ca	^{36}Ar + ^{28}Si
E_{beam} =96MeV	E_{beam} =148MeV
Backet target	Thin target
Euroball { 26 Clovers / 15 Clusters	Gammasphere (87 Ge) / Microball
ISIS 40 SiΔE−E	Si−strip telescope
Neutron Wall	20 neutron detectors

Table 2. Characteristics of the new experiments performed to study ^{59}Cu.

The Euroball set-up involved at that time 26 clover detectors and 15 cluster detectors. It was coupled to the 4π Si ball ISIS [28], which consists of 40 ΔE-E-telescopes, and the dedicated Euroball Neutron Wall [29]. The main goals of the experiment were to determine the lifetimes, the spins, and the parities of the nuclear states belonging to the deformed bands associated with the prompt particle decays in ^{58,59}Cu and ^{56,58}Ni.

The Argonne (GSFMA42) experimental set-up consisted of the Gammasphere array involving 87 Ge detectors together with Microball and four highly segmented ΔE-E-Si-strip telescopes replacing the three most forward rings in Microball. It also involved 20 neutron detectors. We expect it to be 10 times more sensitive to the observation of the prompt discrete-energy proton or α-lines, and to be able to extract more precisely the energies and the branching ratios for the weak particle decay branches.

The GSFMA42 experiment is presently being analyzed and is not part of the present thesis. Results from the Euroball experiment concerning the ^{58}Cu nucleus are presented in the second part of Paper II. The respective data analysis was performed by Dr. D. Rudolph.

Chapter 4

Analysis

4.1 Sorting

The data collected during the experiment are stored on EXABYTE tapes and later on sorted off-line using adequate programs. After a presorting procedure, which reduces considerably the data volume, the sorting procedure starts. This implies that the channel of interest is selected by gating with the proper number of evaporated particles. The events are sorted into symmetrized E_γ-E_γ matrices and E_γ-E_γ-E_γ cubes.

A γ-ray multiplicity and γ-ray sum-energy spectrometer consist of a 4π multidetector array of γ-detectors. Gammasphere has the attributes of such a spectrometer, if both the Ge and BGO detectors are considered. If the Heavimet collimators in front of the BGO shields are removed, Gammasphere can determine the γ multiplicity (M_γ) and total γ-ray energy (E_{tot}). The multiplicity measurements for a given event can be made by counting the number of the individual detector elements, which recorded a γ-ray above an instrumental threshold. The resulting number is the fold, k, which is proportional to M_γ. The measurement of the total emitted γ-ray energy, H, of the event is made by summing the observed signals in all Ge and BGO detectors, which is proportional to E_{tot}. This allows for an additional two-dimensional gate H versus k, the so-called Hk-gate.

The Microball detector measures the sum-energy of the particles, E_{part}, in the center-of-mass system. The total particle energy versus total γ-ray energy plot (i.e., the E_{part} versus H) should show a straight line, because the excitation energy of the compound nucleus is nearly constant. For the 2α1p-channel corresponding to ^{59}Cu the main contamination comes from the 2α2p-channel corresponding to ^{58}Ni, when one proton escaped the detection in Microball. In the E_{part} versus H matrix for the 2α1p-channel the contribution from the 2α2p-channel lies on another line below the one corresponding to the 2α1p-channel. The two lines are different, a fact which allows largely to eliminate the contamination from ^{58}Ni in the channel corresponding to ^{59}Cu. These two two-dimensional gates set on the matrix H versus k, and E_{part} versus H are called "Hk gating". The Hk-gate helps to select events from one particular reaction channel, which belongs to a specific isotope, and provide background suppression.

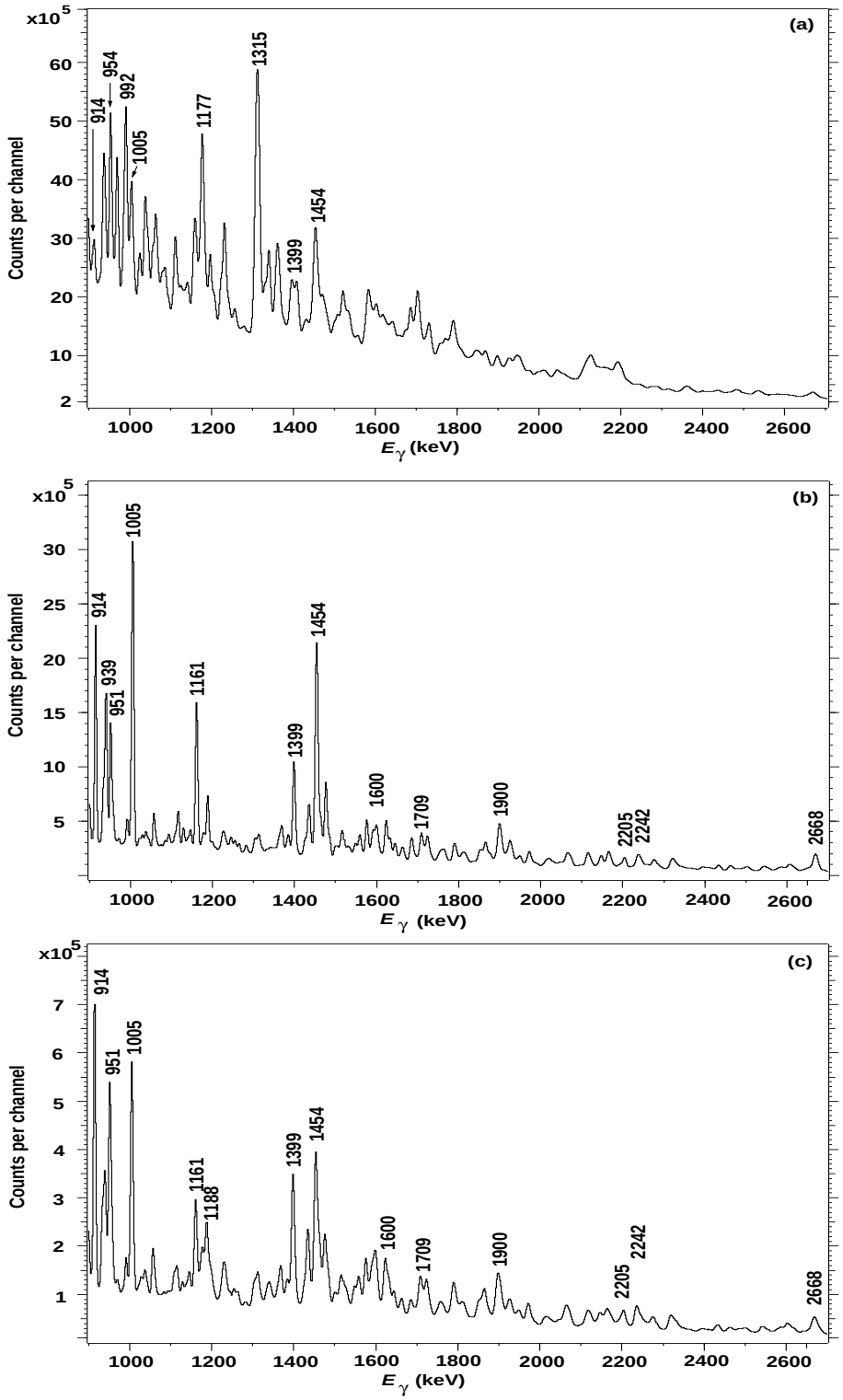

Figure 4.1: Gamma-ray spectra obtained from the GS90 experiment: (a) total projection, (b) 2α1p-gated total projection, (c) 2α1p-Hk-gated total projection. See text for details.

Figure. 4.1 shows three γ-ray total projection spectra obtained from the GS90 experiment. A total projection is obtained by projecting the content of a E_γ-E_γ matrix on one axis. Panel (a) shows a γ-ray total projection with no particle gate, i.e. γ-rays corresponding to all nuclei populated in reaction are present. The number of the counts in this spectrum is very high. The peaks are very broad and they can barely be used for gating. The strongest peak at 1315 keV mostly belongs to ^{64}Zn ($\sigma_{rel} \approx 12\%$), while the peaks at 954 and 1177 keV belong to ^{62}Zn ($\sigma_{rel} \approx 12\%$). For comparison, the peaks at 914 and 1399 keV belonging to ^{59}Cu ($\sigma_{rel} \approx 5\%$) and at 1005 and 1454 keV belonging to ^{58}Ni ($\sigma_{rel} \approx 9\%$) are shown. Panel (b) shows a 2α1p-gated, γ-ray total projection spectrum, while panel (c) shows a 2α1pHk-gated γ-ray total projection spectrum. The differences are obvious. First, one can observe that in the spectrum in Fig. 4.1(b) there are more events, but the strongest transitions at 1005, 1454, and 2668 keV belong to ^{58}Ni, although the 2α1p-particle gate corresponds to ^{59}Cu nucleus. Selecting the Hk-gate corresponding to ^{59}Cu (Fig. 4.1.(c)), the contribution of ^{58}Ni in the 2α1p channel is suppressed and the transitions belonging to ^{59}Cu at 914, 951, 1399 keV are dominant.

4.2 Level Scheme

The useful format for analysis is to sort the data in E_γ-E_γ matrices and E_γ-E_γ-E_γ cubes with appropriate particle gates applied. By setting γ-energy gates in the matrices on one axis and observing the γ-lines in coincidence, the level scheme of the nucleus is built. The high-spin level scheme of ^{59}Cu is shown in Fig. 4.2. Previously, high-spin states in ^{59}Cu were known up to spin and parity $I^\pi = 17/2^-$ at an excitation energy of $E_x = 5722$ keV [30]. The present level scheme of ^{59}Cu was enlarged up to spin and parity $I^\pi = 57/2^+$ at an excitation energy of $E_x = 31.96$ MeV, and it consists of eleven different structures. The band sequencies in the level scheme are labeled with numbers to facilitate their description. The structures 1 to 6 are discussed in Paper I and II, but the results of the structures 7 to 11 have not yet been published. The superdeformed band 1 and 6 are also named B1 and B2, respectively, in order to be consistent with the previous partial level schemes published in Paper I and II.

To reduce the contamination from other (strong) reaction channels, spectra with the same γ-gate but different particle gates can be subtracted from each other to obtain clean spectra. An example is shown in Fig. 4.3. The 1900 keV γ-ray transition is one of the transitions belonging to the superdeformed band 1 in ^{59}Cu, but there is also a 1900 keV line which belongs to ^{58}Ni. Figures 4.3(a) and (b) respectively, show the 2α1pHk- and 2α2pHk-gated spectra in coincidence with the 1900 keV γ-ray transition. The spectrum in Fig. 4.3(b) is normalized with a factor of 0.37, which is obtained from the ratio of the intensities of the 1005 keV transition in spectrum (a) and (b). The normalized 2α2pHk-gated spectrum is subtracted from the 2α1pHk-gated spectrum, and the result is shown in Fig. 4.3(c). The improvement is observed by comparing the transitions belonging to ^{59}Cu, which now are stronger. The γ-ray transition at 1005 keV belonging to ^{58}Ni disappeared.

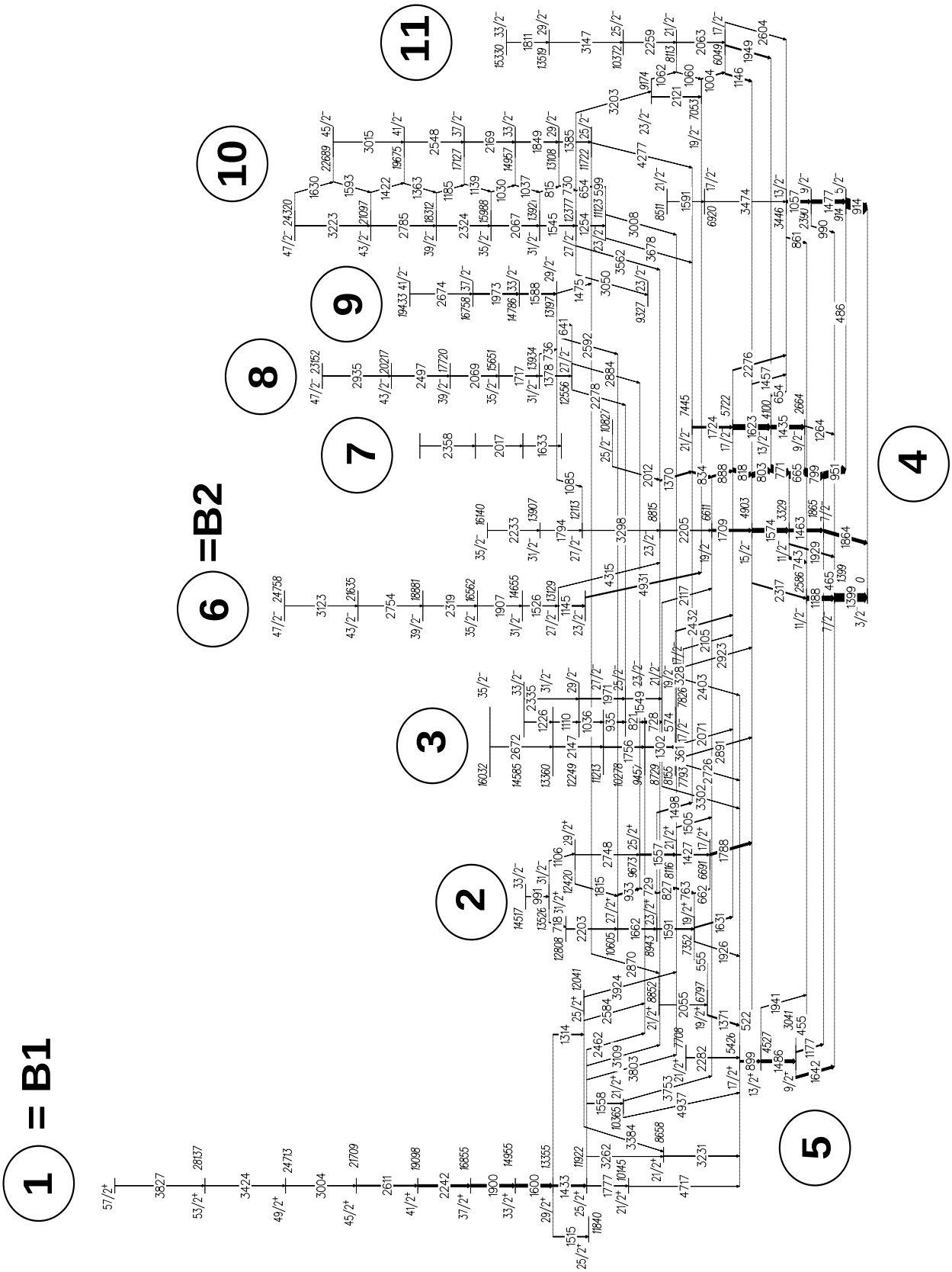

Figure 4.2: Proposed level scheme of ^{59}Cu.

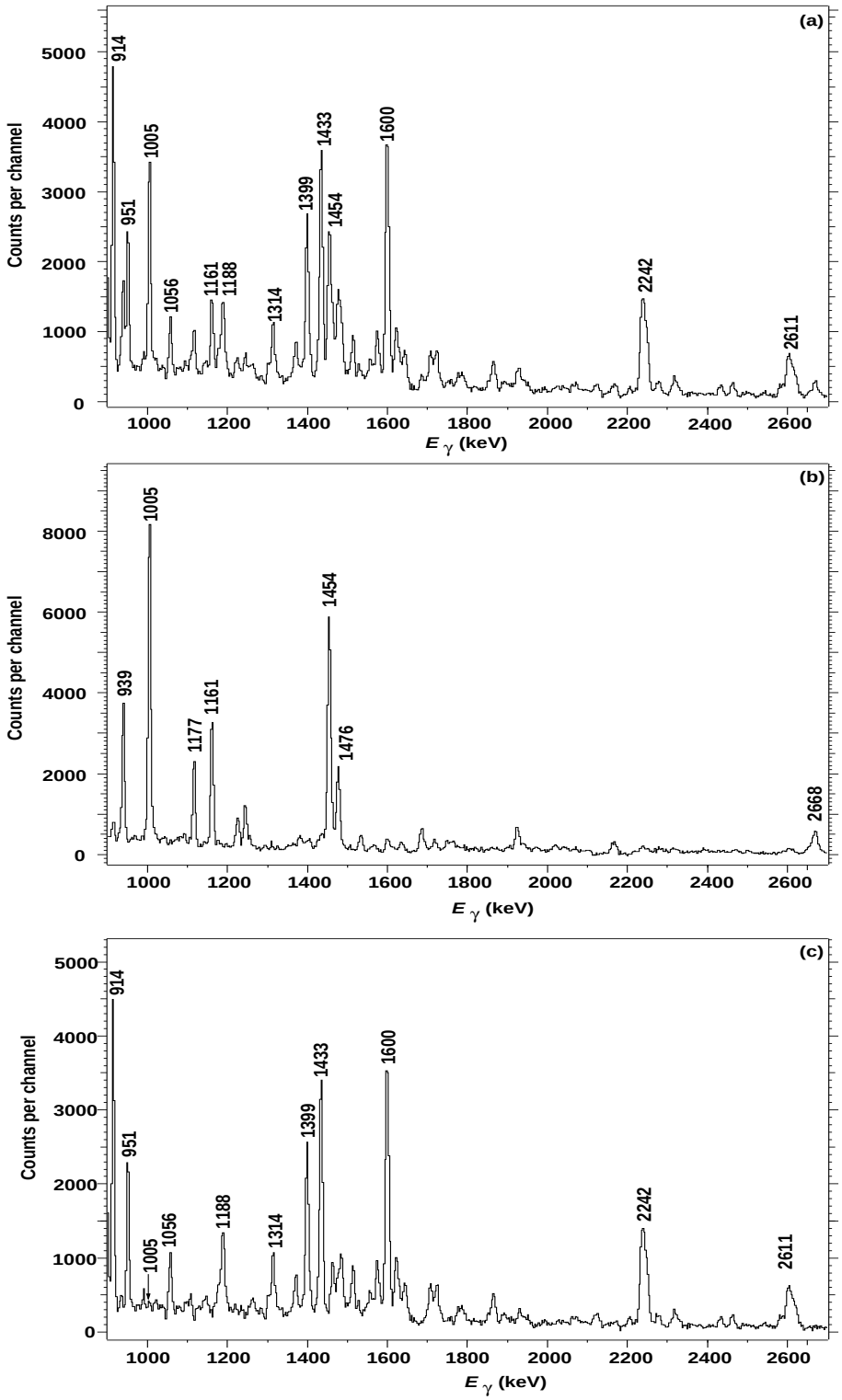

Figure 4.3: Three γ-ray spectra in coincidence with the transition at 1900 keV obtained from the GS90 experiment: (a) $2\alpha 1\mathrm{p}Hk$-gated, (b) $2\alpha 2\mathrm{p}Hk$-gated, and for (c) a fraction of (b) was subtracted from spectrum (a). See text for details.

Figure 4.4 shows four 2α1pHk-gated γ-ray spectra from the GS90 experiment. The transitions in the spectrum of panel (a) of Fig. 4.4 are in coincidence with the 328 keV line, which is situated at the bottom of the right branch of band 3. It depopulates the state at an excitation energy of 8154 keV. The 328 keV line is coincident with the 575, 728, 821, 935, 1036, 1302, 1549, 1757, 1971, and 2147 keV lines, which are well represented in this spectrum. The transitions at 2105 and 2923 keV connect the 7826 keV state in band 3 with two states in band 4 at 5722 and 4903 keV, respectively. The transitions in the spectrum shown in Fig. 4.4(b) are in coincidence with the 361 keV line, which depopulates the same 8154 keV state as the 328 keV line. The 361 keV line at the bottom of the left branch of band 3 is coincident with the same chain of transitions as the 328 keV line, except the transitions at 2071 and 2891 keV, which connect the state at 7793 keV in band 3 with the same two states at 5722 and 4903 keV, respectively. From spectrum (a) and (b) we can say that the 328 and 361 keV lines are not coincident with one another, but both are coincident with the 575 keV line, which is the strongest line in these spectra. The next step is to look at transitions coincident with the 575 keV line, which are illustrated in the spectrum in Fig. 4.4(c). Our assumption is correct and we can see that the 575 keV line is coincident with the lines at 328 and 361 keV. The transitions at 2071, 2105, 2891, and 2923 keV, which connect band 3 and 4 are also in coincidence with the 575 keV line. The strongest transition in coincidence with the 575 keV line is the 728 keV line, which is the next transition in band 3. The spectrum in Fig. 4.4(d), gated on the 728 keV transition, confirms that the 328 and 361 keV lines depopulate the same level, and that they are both in coincidence with the 575 and 728 keV lines. In this manner, band 3 was connected with band 4, and its excitation energy was extended till 16031 keV. The same procedure was used to extend the entire level scheme in Fig. 4.2. The analysis is based also on a 2α1p-gated E_γ-E_γ-E_γ cube, which is able to provide spectra generated by summing double gates in multiple combinations.

The next step is to assign the spins and parities for the new states in the level scheme. The assignment of the multipolarities of γ-ray transitions can be done using directional correlations from oriented states (DCO ratios) [31]. For this purpose, the Ge detectors in Gammasphere were grouped into two "pseudo" rings labeled '30°' (15 detectors at 142.6°, 148.3°, and 162.7°) and '83°' (25 detectors at 79.2°, 80.7°, 90.0°, 99.3°, and 100.8°) [3]. A 2α1p-gated $E_\gamma - E_\gamma$ matrix with γ-rays detected at 30° sorted on one axis and 83° on the other axis was created. From this matrix DCO-ratios R_{DCO} were extracted [31] according to the given formula

$$R_{DCO}(\text{30-83};\gamma_1,\gamma_2) = \frac{I(\gamma_1 \text{ at } 30°;\ \text{gated with } \gamma_2 \text{ at } 83°)}{I(\gamma_1 \text{ at } 83°;\ \text{gated with } \gamma_2 \text{ at } 30°)}. \tag{4.1}$$

Known stretched $E2$ transitions were used for gating. For observed stretched $\Delta I = 2$ transitions $R_{DCO} \approx 1.0$ is expected, while pure stretched $\Delta I = 1$ transitions have $R_{DCO} \approx 0.6$. However, $\Delta I = 1$ transitions can show deviations from the expected value due to quadrupole admixtures i.e., non-zero $\delta(E2/M1)$ mixing ratios ($M2$ admixtures into $E1$ dipoles are not likely). DCO ratios for some γ-ray transitions are shown in Table 1 of Paper I.

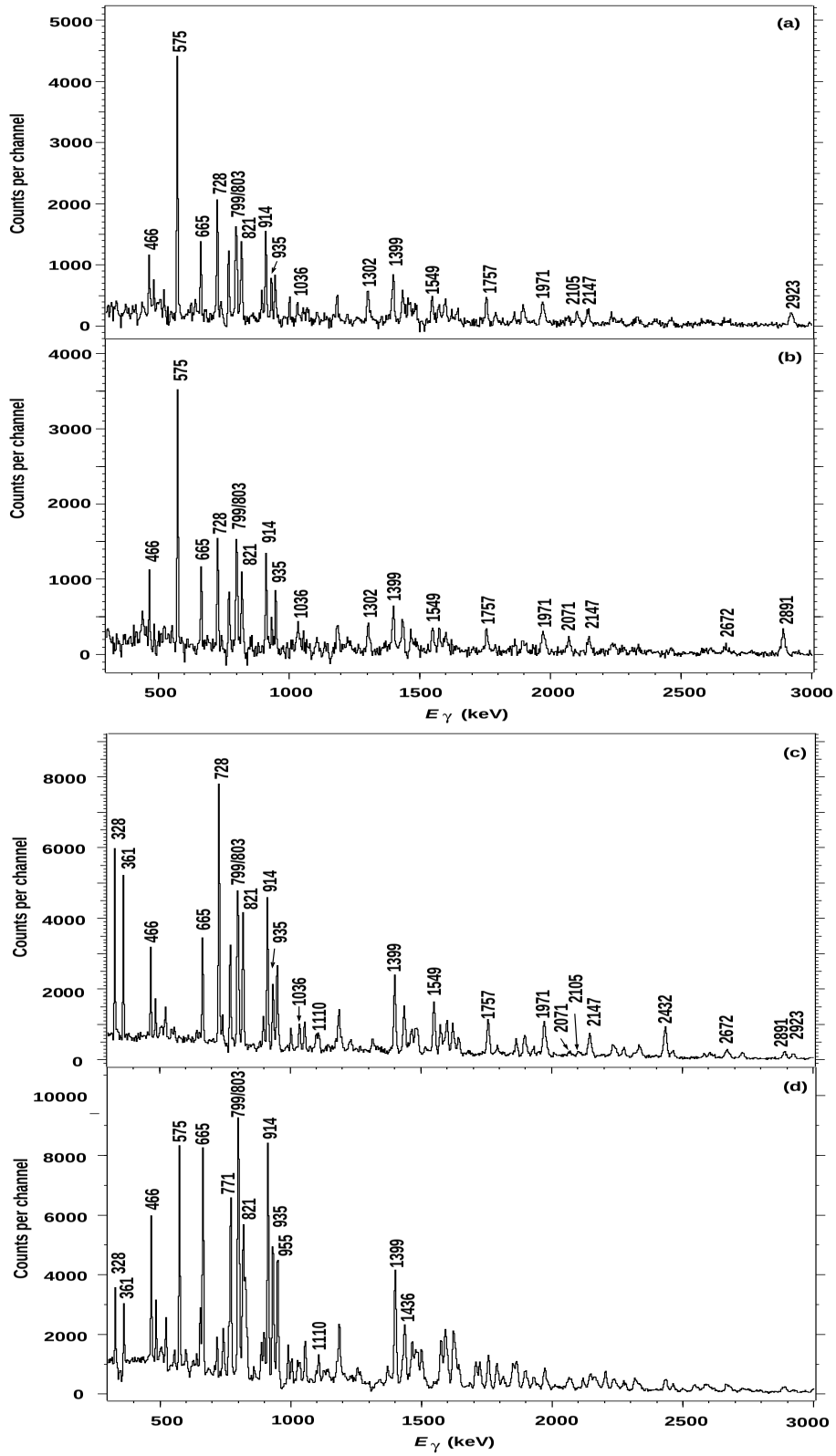

Figure 4.4: Four $2\alpha 1\mathrm{p}Hk$-gated γ-ray spectra in coincidence with (a) the 328 keV line, (b) the 361 keV line, (c) the 575 keV line, and (d) the 728 keV line.

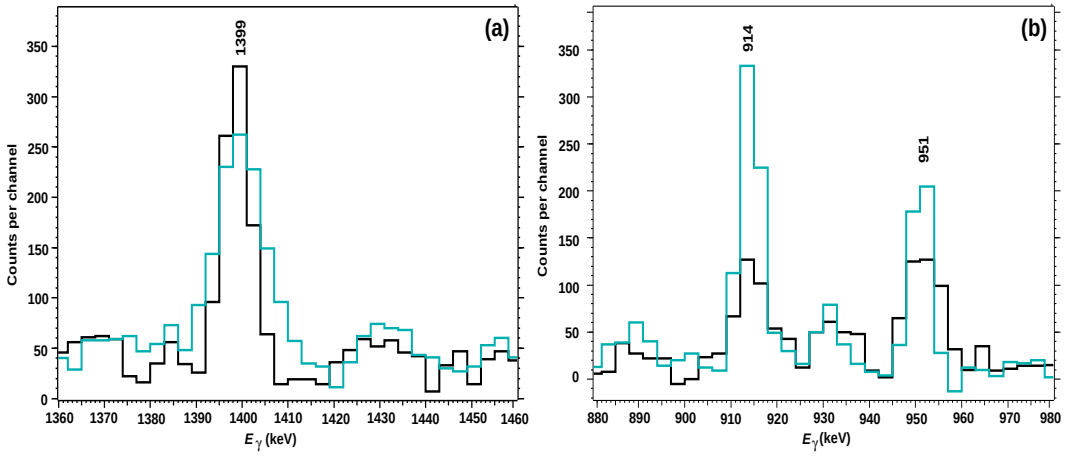

Figure 4.5: Two 2α1p-gated γ-ray spectra with γ rays detected at 30° sorted on one axis and 83° on the other axis, gated on (a) 1188 keV $11/2^- \rightarrow 7/2^-$ line and (b) the 1574 keV $15/2^- \rightarrow 11/2^-$ line.

In Fig. 4.5(a) are two spectra obtained from a 2α1p-gated E_γ-E_γ matrix with γ-rays detected at 30° sorted on the x-axis and 83° on the y-axis. The two spectra are generated by gating on the 1188 keV $11/2^- \rightarrow 7/2^-$ transition. The black spectrum is obtained by gating on the y-axis and projecting the events onto the x-axis. The grey spectrum is produced in the opposite way. The 1399 keV line has a stretched $\Delta I = 2$ character, which can already be seen by observing that the 1399 keV peak has basically the same intensity in both spectra ($R_{DCO} \approx 1.0$). The value of a R_{DCO} ratio is obtained by fitting the peaks present in each spectrum, dividing their intensities and then correcting the result with the γ-ray efficiency. The spectra shown in Fig. 4.5(b) are obtained in a similar way as described above, but they are gated on the 1574 keV $15/2^- \rightarrow 11/2^-$ transition. The transitions at 914 and 951 keV are stretched $\Delta I = 1$ transitions. The peaks in the grey spectrum at 30° have higher intensities than in the black spectrum at 83°. If the transitions have a mixed $E2/M1$ character, the R_{DCO} ratios have values which deviate from the expected value of $R_{DCO} \approx 0.6$. For example, this is the case for the 2585 keV line as described in Paper I. This implies that the 2585 keV line does not change the parity of the states which it connects.

4.3 Superdeformed States

How can one prove that a band is superdeformed? Because of the high collectivity and high transition energies of superdeformed bands in the mass $A \sim 60$ region, the lifetimes of the states are much shorter than the maximum time it takes for the recoiling nucleus to pass through the thin target (t $\sim$ 170 fs). Almost the entire band thus decays while the nucleus is slowing down in the thin target. This leads to

additional Doppler shifts of the peaks in the γ-ray spectra of Ge-detectors at forward (50°) and backward angles (130°), because the Doppler correction is performed with an average velocity of the recoils after the target. The observation of such shifts is an excellent tool to prove that the transitions actually belong to a superdeformed band [32].

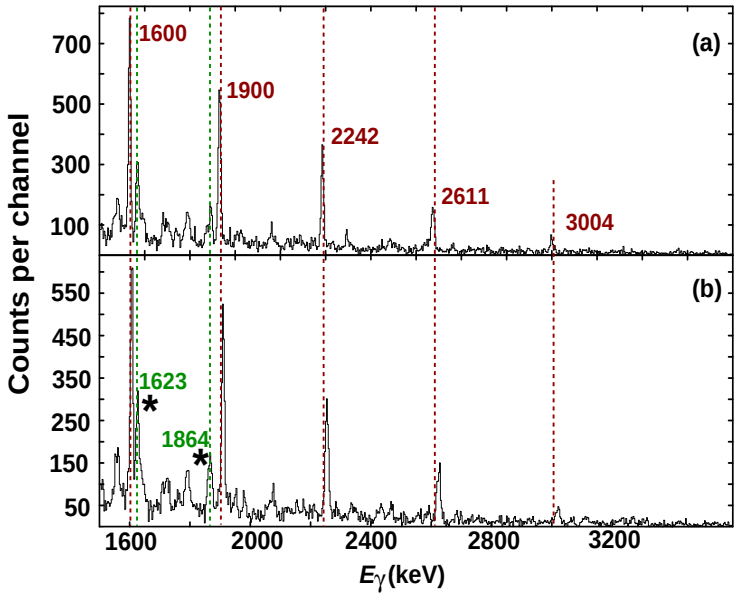

Figure 4.6: Two gamma-ray spectra in coincidence with the 1433 keV transition at (a) 130° and (b) 50° detector angles. Note the increasing additional Doppler shifts of the transitions belonging to the superdeformed band with increasing gamma-ray energy.

Figure 4.6 shows two spectra in coincidence with the 1433 keV transition of band 1 in the Ge-detectors at 130° [panel (a)] and 50° [panel (b)]. One can see that the transitions belonging to the superdeformed band are shifted. The transitions which do not have any shifts (marked with stars) are decaying from states which live longer. These states are the normally deformed states.

A systematic analysis of these shifts is called the fractional Doppler shift method [32]. It is described in Paper I for the case of band 1 in ^{59}Cu. The measurements of the fractional Doppler shifts and deduced $F(\tau)$ values for the transitions in band 1 were based on the spectra in Fig. 4.6. The states towards the top of the band decay faster than states at the bottom of the band. This is illustrated by the increasing additional Doppler shift of the transitions in the band with increasing γ-ray energy. Band 1 is best fit by $Q_t = 2.24 \pm 0.40$ eb in the spin range 29/2-49/2 $\hbar$ (see Paper I).

4.4 Linking Transitions

It is very important to observe experimentally the linking transitions which are connecting the superdeformed band with the normally deformed states. They are typically very weak, only a few percent relative to the transitions of the superdeformed band. They allow to define the excitation energy, the spin, and the parity of the superdeformed band. Band 7 in the level scheme of ^{59}Cu in Fig. 4.2 is an example of a band which has not yet been linked.

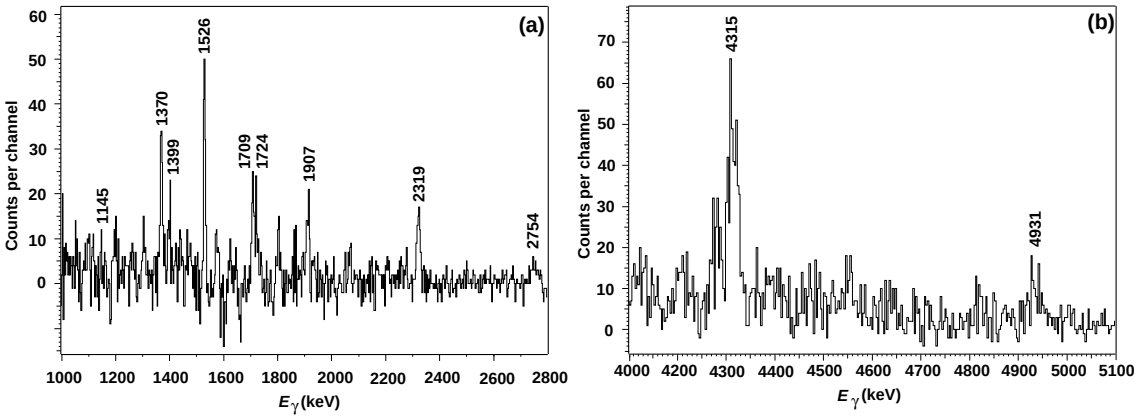

Figure 4.7: (a) Gamma-ray spectrum from the GS90 experiment generated by gating on the 4315 keV transition. It shows the γ-ray transitions in band 6. (b) Gamma-ray spectrum from the GS90 experiment generated by summing all double gates set on the transitions in band 6, showing the two linking transition of band 6 at 4315 and 4931 keV.

Figure 4.7 shows two 2α1p-gated γ-ray spectra obtained from the GS90 experiment. The spectrum in Fig. 4.7(a) is in coincidence with the 4315 keV line and shows the superdeformed band 6, except for the 1145 keV line. The 1145 keV line is not coincident with the 4315 keV line, as they both depopulate the same level at an excitation energy of 13129 keV. The spectrum in Fig. 4.7(b) is generated by summing all double gates set on the transitions belonging to band 6, and shows the two linking transitions of band 6 at 4315 and 4931 keV. The 4931 keV line is coincident with 1145 keV and connects the bottom of band 6 with the 7053 keV state.

4.5 Prompt Proton Decays

The intensity of the superdeformed band B1 in ^{59}Cu relative to the 1399 keV line ground-state transition is about 30%. About half of this intensity is carried by the observed weak linking transitions. The missing intensity of the linking transitions from the superdeformed states in ^{59}Cu was partially recovered into the prompt proton decay from this band towards the normally deformed states in the daughter

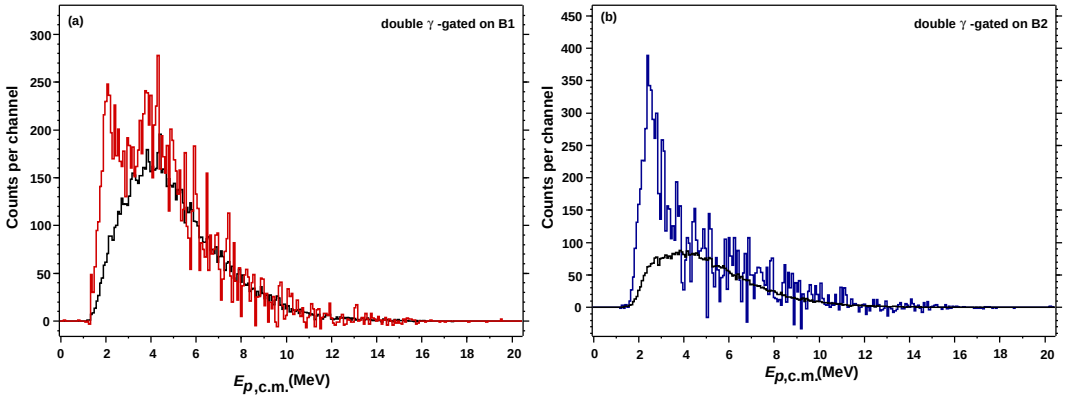

Figure 4.8: (a) Two proton spectra obtained from a $2\alpha 2p$-gated E_γ-E_γ-$E_{p,c.m.}$ cube, double gated with γ-ray transitions belonging to band B1 (top panel) and band B2 (bottom panel). Normalized evaporation spectra of the protons following the fusion-evaporation reaction are overlaid.

nucleus ^{58}Ni. The strong direct evidence of prompt proton decay in ^{59}Cu (see also Fig. 2. in Paper II) are proton spectra obtained from the 2α2p-gated E_γ-E_γ-$E_{p,c.m.}$ cube. The spectrum in Fig. 4.8(a) is the sum of spectra gated by the 1433, 1600, 2242, 2611, and 3004 keV transitions. A peak-like structure at the proton energy of $E_{p,c.m.} = 2.0(1)$ MeV appears. The overlapping spectrum represents the normalized total projection of the E_γ-E_γ-$E_{p,c.m.}$ cube. The shape of the total projection reflects the expected distribution of the proton energies following the fusion-evaporation reactions. The normalized evaporation spectrum of the protons was subtracted from the spectrum of the protons in coincidence with the transitions belonging to band B1. The new spectrum revealed a proton peak at $E_{p,c.m.} = 2.0(1)$ MeV. The explanation of Fig. 4.8(b) is similar, but it illustrates the proton peak associated with band B2 at $E_{p,c.m.} = 2.5(1)$ MeV. The analysis was done in the same manner as described for band B1. The data used in this analysis are sorted in $2\alpha 2p$-gated E_γ-E_γ matrices without Hk-gates because we do not want to eliminate the events belonging to the ^{59}Cu nucleus, but to observe the proton emission into ^{58}Ni. The protons are only detected in the first forward rings of Microball. Beyond the fourth ring of Microball, the laboratory energy of the proton peak starts merging into the energy threshold of the Microball CsI detector.

More evidence for the prompt proton decay arises from the investigation of a 2α2p-gated E_γ-E_γ matrix with and without an additional restriction for the proton of $E_{p,c.m.} < 3.0$ MeV in the case of band B2. The explanation is similar for band B1, but the proton energetical restriction was $E_{p,c.m.} < 2.7$ MeV. Figure 4.9 shows γ-ray spectra with the proton energetical restriction imposed. The energy restriction eliminates 88% of the evaporation protons with energies in excess of 3.0 MeV for band B2 and shows into which spherical states in ^{58}Ni the protons associated with band B2 are decaying. In the spectrum in Fig. 4.9(b) one can observe the transitions belonging to band B2 in ^{59}Cu and γ-ray transitions belonging to ^{58}Ni are marked

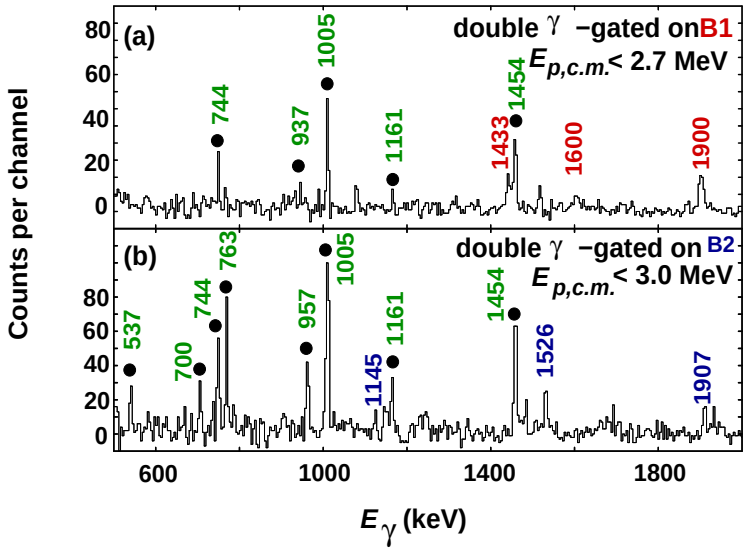

Figure 4.9: Gamma-ray spectra obtained from a $2\alpha 2p$-gated E_γ-E_γ-E_γ cube. They are sums of spectra double gated with γ-ray transitions belonging to band B1 (top panel) and band B2 (bottom panel). At least one proton has to have the energy $E_{p,c.m.} < 2.7$ MeV (band B1) and $E_{p,c.m.} < 3.0$ MeV (band B2).

with circles. The transitions at 700 and 957 keV indicate that the proton emitted from band B2 populates the yrast 7^- state in ^{58}Ni. The spherical state in ^{58}Ni at 9883 keV, depopulated by the 957 and 700 keV lines match also with the energy difference between the excitation energies of band B2 and the energies of the emitted proton. In the spectrum in Fig. 4.9(a), one can observe the transition belonging to band B1 in ^{59}Cu and γ-ray transitions belonging to ^{58}Ni marked with black circles. The transition 937 keV indicates that the proton emitted from band B1 feeds the yrast 8^+ state in ^{58}Ni. A relaxed energy restriction of $E_{p,c.m.} < 4.0$ MeV revealed also the 537 keV transition which was expected to support the presence of the 937 keV line.

The intermediate stages described in this paragraph complete the detailed description of steps followed for the verification of the prompt proton decays done in Paper II.

Chapter 5

Discussion

5.1 Configuration of the Superdeformed Bands

In the Nilsson scheme, illustrated in Fig. 2.1, each level can be occupied by two neutrons. The protons occupy the same orbitals in a similar proton single-particle level diagram. At zero deformation for ^{56}Ni the levels are filled up to the $f_{7/2}$ shell. It means eight neutrons and eight protons above the doubly-magic core ^{40}Ca. At a deformation of $\beta_2 \sim 0.4$ the filling of the single-particle levels is changed by the upsloping of the [303]7/2 orbit and downsloping of the [321]1/2 orbit. The two neutrons from the [303]7/2 orbit will occupy the [321]1/2 orbit, leading to two neutron holes in the $f_{7/2}$ orbit and two neutrons in the $p_{3/2}$ orbit. One can observe that the $g_{9/2}$ orbit is the first available orbital to add neutrons at the deformed shell closure at particle number 28. For a $N = Z$ nucleus, the protons occupy the same orbitals as the neutrons. The configuration of the deformed band in the $N = Z = 29$ nucleus ^{58}Cu is thus four holes in the $f_{7/2}$ orbit four particles in (fp) shell, which consists of the $2p_{3/2}$, $1f_{5/2}$, and $2p_{1/2}$ orbits, and two particles (one proton and one neutron) in the $g_{9/2}$ orbit. The superdeformed band in ^{59}Cu has two neutrons and one proton in excess of ^{56}Ni, so these three particles will occupy the $g_{9/2}$ orbit. In general, the configurations of the superdeformed bands belonging to the mass $A \sim 60$ region are expected to have the leading component $f_{7/2}^{-4} \otimes (fp)^4 \otimes g_{9/2}^{A-56}$ (A-56 is the number of nucleons in excess of ^{56}Ni) with respect to the doubly-magic ^{56}Ni $N = Z = 28$ spherical core. Due to the limited number of valence particles, the low-spin states of ^{59}Cu can be interpreted in the spherical shell-model framework as in the other neighboring nuclei [33].

5.2 Theoretical Comparisons

The discovery of the superdeformed bands in the mass $A \sim 60$ region in different Ni, Cu and Zn isotopes has allowed us to compare the features of the superdeformed bands in ^{58,59}Cu and ^{60}Zn. The input parameters for simple cranking model calculations [34, 35] are spins, excitation energies of the states in the band of interest, and the projection of the angular momentum on the symmetry axis K. The angular

velocity of the rotation is defined as

$$\omega(I) = \frac{1}{\hbar}\frac{dE(I)}{dI_x} \tag{5.1}$$

where I_x is the component of the angular momentum along the axis of rotation. The relation between I_x and the total angular momentum is

$$I_x = \sqrt{I(I+1) - K^2} \approx \sqrt{(I+1/2)^2 - K^2} \tag{5.2}$$

For discrete variation of $E(I)$, the rotational frequency becomes

$$\omega(I) = \frac{1}{\hbar}\frac{E(I+1) - E(I-1)}{I_x(I+1) - I_x(I-1)} \tag{5.3}$$

which reflects the discrete nature of the angular momentum I. The kinematical moment of inertia $J^{(1)}$ is expressed as the first derivative of the energy

$$J^{(1)} = \left(\frac{2}{\hbar}\frac{dE(I)}{d(I_x^2)}\right)^{-1} = \hbar\frac{I_x}{\omega(I)} \tag{5.4}$$

and the dynamic moment of inertia $J^{(2)}$ is expressed as the second derivative of the energy, which gives "the curvature" of the $E(I)$ line

$$J^{(2)} = \left(\frac{1}{\hbar^2}\frac{d^2E(I)}{dI_x^2}\right)^{-1} = \hbar\frac{dI_x}{d\omega(I)}. \tag{5.5}$$

The relative alignment $i(\omega)$ is defined as the difference between the actual yrast angular momentum $I_x(\omega)$ and an auxiliary $I_{ref}(\omega)$ which is called the reference rotor

$$i(\omega) = I_x(\omega) - I_{ref}(\omega). \tag{5.6}$$

In our calculations the reference rotor was the ^{58}Cu nucleus.

In the Cranked Nilsson Strutinsky (CNS) approach the total energy is described as a sum of the liquid drop energy and the shell correction energy. This approach provides a good description of the many-body problem. In CNS calculations for the mass $A \sim 60$ [36] the Nilsson potential with standard set of parameters is used. Pairing correlations are not taken into account at high angular momentum. The configurations can be specified not only by the number of particles in the orbitals of different parity and signature, but also by the number of particles in different N-shells. These calculations were performed by Professor I. Ragnarsson.

The cranked relativistic mean field (CRMF) theory [37] was also employed for theoretical comparison with the experimental data. In the relativistic mean field (RMF) theory the nucleus is described as a system of pointlike nucleons represented by Dirac spinors and coupled to mesons and to the photon. The nucleons interact by the exchange of several mesons, namely, the scalar meson σ and three vector particles: ω, ρ and the photon. CRMF theory is a fully self-consistent theory.

For ^{59}Cu the NL3 interaction [38] was used. These calculations were performed by Dr. A. V. Afanasjev.

In the Hartree-Fock mean-field theory the nucleons move independently from each other in an average potential with a large mean-free path. The nucleon-nucleon interactions that are of zero-range in coordinate space but at the same time are density- and velocity dependent are called Skyrme effective interactions. The theoretical Hartree-Fock calculations [39] in Paper I are based on the SLy4 force [40]. They were performed by Professor J. Dobaczewski.

Figure 5.1 shows the kinematical moments of inertia for the rotational bands in ^{58,59}Cu and ^{60}Zn. The top panel presents the experimental kinematical moments of inertia obtained from equations (5.3) and (5.4). Starting from ^{58}Cu, which has one proton and one neutron in the $g_{9/2}$ orbital, the moment of inertia increases for ^{59}Cu, which has one proton and two neutrons in the $g_{9/2}$ orbital. The addition of one more proton in the $g_{9/2}$ orbital corresponding to ^{60}Zn increases the moment of inertia even further. This increase in $J^{(1)}$ is due to an increase in deformation. The deformation driving character of the $g_{9/2}$ orbital is nicely illustrated and one can observe that ^{59}Cu is placed in between ^{58}Cu and ^{60}Zn.

In the bottom panel the experimental values of ^{59}Cu are compared with theoretical predictions. They are in very good agreement, especially for the CNS predictions. None of the theoretical calculations include pairing, and thus are realistic only at relatively high spin. The HF approach overestimate the moment of inertia, which might be improved when standard $T = 1$ pairing correlations are taken into account. The comparison of the dynamic moments of inertia $J^{(2)}$ for the ^{58,59}Cu and the ^{60,61}Zn nuclei for several collective bands (see Fig. 3, Paper I) shows also that the quadrupole deformation of these bands increase with the number of $g_{9/2}$ particles involved in their configurations. There is a smooth increase of β_2 from 0.37 to 0.51, when going from ^{58}Cu to ^{60}Zn.

The study of $N \approx Z$ nuclei could elucidate the role of neutron-proton pairing correlations, since both types of nucleons involved in the band configurations occupy the same orbitals. The dynamic moments of inertia $J^{(2)}$ of the $N = Z$ nuclei ^{60}Zn and ^{58}Cu were compared with the recently observed neighboring $N = Z + 1$ nuclei ^{61}Zn and ^{59}Cu. The simultaneous alignment of the $g_{9/2}$ protons and neutrons in ^{60}Zn reveals a band crossing at a rotational frequency $\hbar\omega \approx 1$ MeV. The investigation of ^{59}Cu did not reveal the expected neutron alignment present in ^{60}Zn. Like in the odd-neutron neighbor ^{61}Zn, it is either absent or shifted to lower frequencies. This effect may be attributed to $T = 0$ pairing, possibly influenced by a change of deformation determined by the number of the $g_{9/2}$ particles involved in the band configurations.

5.3 Linking Transitions and Decay-Out Mechanism

The linking transitions may not only provide the excitation energies, definite spins, and parities of the superdeformed bands but will give information about the decay-

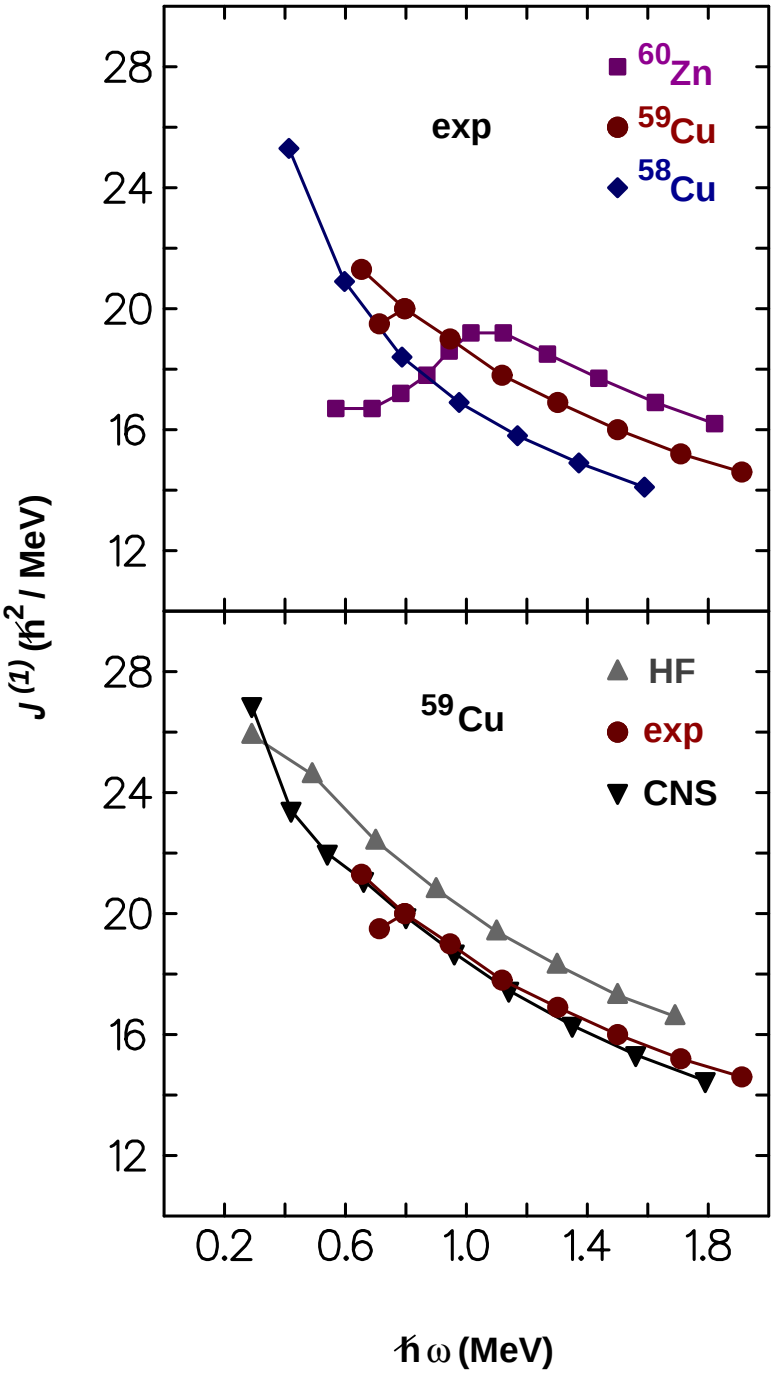

Figure 5.1: The kinematical moments of inertia for the superdeformed bands in ^{58,59}Cu and ^{60}Zn.

out process. ^{59}Cu is the second nucleus in the mass $A \sim 60$ region which has a superdeformed band fully characterized with excitation energies, spins, and parities. In the first case, ^{60}Zn, the competition between $E1$, $M1$, and $E2$ decay-out transitions may be influenced by the suppression of isoscalar dipole transitions. The stretched $E2$ character of the linking transitions and the low level density of the states in the first minimum suggest that the decay-out process is non-statistical for this $N = Z$ nucleus [15].

The decay-out in the mass $A \sim 60$ region differs substantially from that which has been observed for the superdeformed bands in the mercury region [41]. In the mass $A \sim 190$ region the linking transitions have provided a consistent description of the decay-out of superdeformed bands as a statistical process governed by the weak mixing of the superdeformed states with the surrounding sea of hot normally deformed states separated by a potential barrier [41]. In such a process one expects a highly fragmented decay mostly by dipole transitions.

Also in the mass $A \sim 130$ region a number a highly deformed bands decay-out through stretched $E2$ transitions. In these nuclei a considerably mixing of the highly deformed ($\beta_2 \sim 0.3 - 0.4$) and normally deformed ($\beta_2 \sim 0.2 - 0.3$) bands to which they decay is understood in terms of their similar deformations and the predicted absence of a barrier between them at the decay-out point.

An alternative explanation for the sudden decay-out of the superdeformed states in the mass $A = 150 - 190$ region is related with the transition from order to chaos [42]. The chaos in the nucleus sets in as the excitation energy increases. For example, the states close to the yrast line are regular, while the states at an energy of 6-7 MeV above yrast are chaotic. As it was explained before, the superdeformed and normally deformed states are separated by a barrier and the decay-out takes place with a dramatic change in nuclear shape. The wave functions describing the two types of shapes are very different. The superdeformed band sees a surrounding of normally deformed states which character changes from order to chaos, as the angular momentum decreases. The decay-out is connected to a tunneling process which occurs through large amplitude vibrational coupling in the quadrupole direction. By this process the wave function describing the superdeformed state picks up a small fraction of states with normally deformed character, while the barrier envelop have strongest couplings. This implies that the decay is restricted to occur between superdeformed and normally deformed states with a special character. This coupling between the normally deformed states and superdeformed states forms a "doorway state" for the decay-out process. By the additional coupling between the normally deformed states the tunneling strength-function spreads out, and the decay from the superdeformed state can occur to a multitude of normally deformed states. It may expect that the decay-out of the superdeformed band is related to the onset of chaos among the normally deformed states, which enhances the decay-out process.

^{59}Cu is a $N \sim Z$ nucleus, in which the decay-out from the superdeformed band takes place through one step stretched $E2$ transitions and $E1$ transitions. The level density of the states in the first minimum of the potential is higher than in the case of the $N = Z = 30$ nucleus ^{60}Zn. Also the intensity of the superdeformed band in ^{59}Cu is not completely recovered by the linking transitions and the prompt

proton decay. It means that more linking transitions might be expected, which so far are unobserved. Their observation would help to give more information about the decay-out mechanism, about the mixing of the superdeformed states with the normally deformed states, and the transition from order to chaos.

5.4 Prompt Proton Decays

Prompt monoenergetic proton and α decay lines were observed in the mass $A \sim 60$ region in the decay of high-spin states situated in a deformed secondary minimum of the nuclear potential into spherical states of the corresponding daughter nucleus. They compete with γ-ray emission towards normally deformed states in the first minimum of the same nucleus.

This process is accompanied by a dramatic change in the nuclear shape which has not yet been accounted for from a theoretical point of view. One of the first attempts was done by P. Talou [43] by using a time-dependent approach based on the numerical solution of the time-dependent Schrödinger equation for the prompt proton decay from a deformed second minimum in ^{58}Cu into an excited state in ^{57}Ni. The advantage of this dynamical approach in comparison to other stationary approaches is that it allows the study of problems where the interaction potential is time-dependent. The time-dependence of the nuclear deformation and of the single-particle potential are considered to follow a linear behaviour, while the nucleus goes from its initial configuration to the final one. As expected, the tunneling probabilities and the decay rates for different time-dependent scenarios depend on the time-dependent single-particle potential. The tunneling angular distribution with respect to the z-axis strongly depends on deformation.

In order to compare the ^{59}Cu prompt proton decay with theoretical interpretation in the framework of the stationary Schrödinger equation, either the proton decay width or the lifetime of the initial state involved in the decay-out process should be known. We hope to determine the angular distribution of the protons with respect to the angular momentum axis from the analysis of the GSFMA42 experiment.

Even if the first step towards a theoretical understanding of this complex particle decay process was done, further and more realistic calculations are necessary.

Chapter 6

Conclusions and Outlook

The level scheme of ^{59}Cu was greatly enlarged and the yrast superdeformed band was identified. This band was fully characterized by excitation energy, spin, and parity. It was also compared to similar bands of ^{58}Cu and ^{60}Zn, both from theoretical and experimental points of view. Among the depicted bands of the level scheme, a second superdeformed band was also observed, linked to the normal deformed yrast states and characterized by excitation energy, spin, and parity. In addition nine more structures were observed in ^{59}Cu.

Both superdeformed bands were found to decay via prompt proton decay towards spherical states of the daughter nucleus ^{58}Ni, in competition with γ-ray emission towards low-spin spherical states in ^{59}Cu. The protons associated with these bands have energies of 2.0 and 2.5 MeV, and feed the 8^+ and 7^- yrast states of ^{58}Ni with branching ratios of 4% and 16%, respectively.

The mass $A \sim 60$ region is a very complex region, and a large variety of nuclear structure phenomena can be experimentally investigated, explained, and compared with theoretical models. Figure 6.1 schematically presents some interesting phenomena which already have been studied. They range from shell-model states near the doubly magic core ^{56}Ni towards the deformed and superdeformed bands, which may reach termination or may decay via prompt particle emission with a dramatical change in the nuclear shape. The three $N = Z$ nuclei ^{56}Ni, ^{58}Cu, and ^{60}Zn in the mass $A \sim 60$ region allowed the investigation of paired band crossings and its interpretation in terms of pairing correlation in $N \approx Z$ nuclei.

In the superdeformed band in ^{59}Cu the last state at 31961 keV has spin and parity of $I^\pi = 57/2^+$, while the maximum possible spin which can be created from seven valence particles and four holes is $I_{max} = 65/2\hbar$. It means that only two transitions are missing from the band termination, if we take into account the quadrupole character of the band. It will be very interesting to observe the superdeformed band termination in ^{59}Cu.

The theoretical description of the prompt particle emission is still not satisfactory, and experimental information concerning the states involved in the decay-out process is still lacking. Concerning the ^{59}Cu nucleus it will be interesting to investigate more carefully the details of the two prompt proton decays, such as more precise branching ratios, decay times as well as the fine structure of the potential.

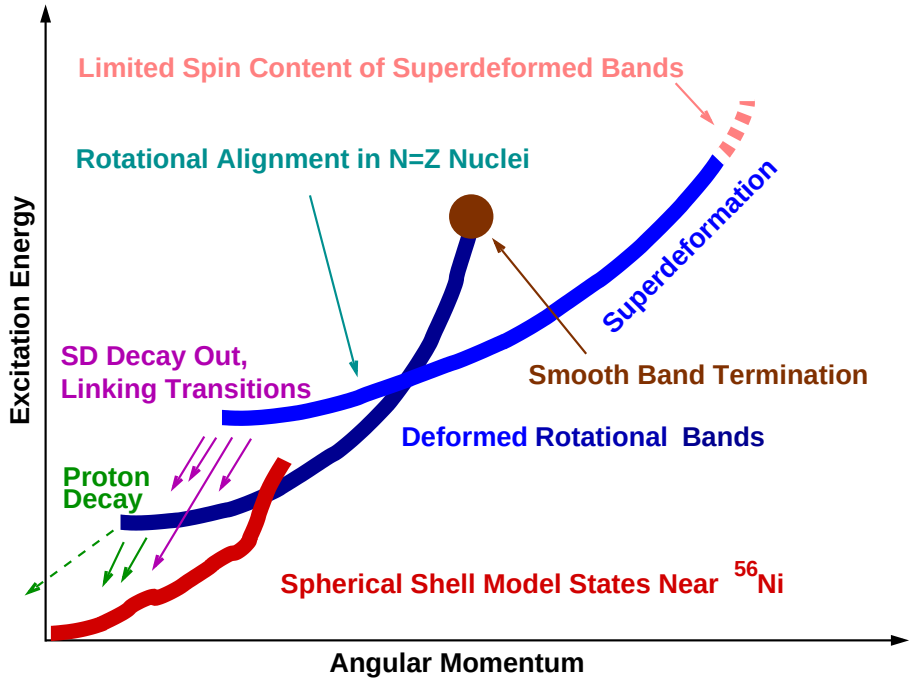

Figure 6.1: Schematic illustration of some nuclear structure effects studied recently in the mass $A \sim 60$ region. Taken from Ref. [44].

These will help to understand the mechanism of the decay-out processes. The high-spin level scheme of ^{59}Cu for sure can be more extended and the new bands need a complete analysis.

Acknowledgements

I would like to thank all members of the Nuclear Structure Group at the Division of Cosmic and Subatomic Physics at Lund University.

First to Prof. Claes Fahlander, who gave me the opportunity to work here and for his precious help during my studies.

Special thanks go to Dr. Dirk Rudolph for his excellent professional support, friendly encouragement and "tough dead-lines". Finally to all the members of the Nuclear Structure Group, namely Prof. Hans Ryde, Dr. Margareta Hellström, Milena Mineva, and Jörgen Ekman for the nice working environment they have created here, for their advises and the useful discussions we have had.

The Mathematical Physics group should be mentioned here for very interesting "nuclear coffee" discussions and seminars. The fruitful collaboration with I. Ragnarsson is gratefully acknowledged.

Also the collaborators who I participated with during the experiments at Legnaro, Italy and Argonne, U.S.A. helped me a lot with their experience.

I am thankful to Dr. Emilian Dragulescu and Dr. Gh. Semenescu from "Horia Hulubei"- National Institute of Physics and Nuclear Engineering Bucharest in Romania, for introducing me into the field of nuclear structure physics.

To all my friends who were there when I most needed them, who shared with me their happy moments and tears, a big hug and many thankful thoughts.

Last, but not least, I am grateful to my family - my husband, Adrian, and my parents - for their endless support and love.

References

[1] http://www.nobel.se

[2] R. Wyss, private communication.

[3] D. Rudolph *et al.*, Eur. Phys. J. A**4**, 115 (1999).

[4] C.E. Svensson *et al.*, Phys. Rev Lett. **82**, 3400 (1999).

[5] S. M. Polikanov *et. al.*, Sov. Phys. JETP **15**, 1016 (1962).

[6] V. M. Strutinsky, Nucl. Phys. **A95**, 420 (1967); **A122**, 1, (1968).

[7] P. J. Twin *et al.* Phys. Rev. Lett. **57**, 811 (1986).

[8] E. F. Moore *et al.* Phys. Rev. Lett. **63**, 360 (1989).

[9] P. J. Nolan *et al.* J. Phys. G **11**, L17 (1985).

[10] C. Baktash, Phys. Rev. Lett. **74**, 1946 (1995).

[11] C.E. Svensson *et al.*, Phys. Rev. Lett. **79**, 1233 (1997).

[12] C.E. Svensson *et al.*, submitted to Phys. Rev. Lett.

[13] D. Rudolph *et al.*, Phys. Rev. Lett. **82**, 3763 (1999).

[14] D. Rudolph *et al.*, Phys. Rev. Lett. **80**, 3018 (1998).

[15] C.-H. Yu *et al.*, Phys. Rev. C**60**, 031305 (1999).

[16] K. P. Jackson, C. U. Cardinal, H. C. Evans, N. A. Jelly, and J. Cerny, Phys. Lett. **B33**, 281 (1970).

[17] D. Rudolph, in *Proceedings of the International Conference on The Nucleus: New Physics for the New Millenium*, January 1999, Faure, South Africa, Eds. F. D. Smit, R. Lindsay, and S. V. Förtsch, Kluwer Academic/Plenum Publishers, New York, 2000, p. 397.

[18] S. Hofmann *et al.*, in *Proc. 4th Intl. Conf. on Nuclei Far from Stability*, CERN 81-09, Geneva, 1981, pp. 190.

[19] D.J. Vieira, D.F. Sherman, M.S. Zisman, R.A. Gough, and J. Cerny, Phys. Lett. **B60**, 261 (1976).

[20] D. Rudolph *et al.*, Phys. Rev. C, to be published.

[21] N. Bohr and F. Kalckar, Det Kgl. Danske Videnskabernes Selskab, Mathematisk-fysiske Meddelelser **XIV**, 10, København, Levin and Munksgaard, 1937.

[22] http://nucalf.physics.fsu.edu/∼riley/gamma/

[23] M. Devlin *et al.*, Nucl. Instrum. Meth. **A383**, 506 (1996).

[24] C.E. Svensson *et al.*, Nucl. Instrum. Meth. **A396**, 288 (1997).

[25] I.-Y. Lee, Nucl. Phys. **A520**, 641c (1990).

[26] EUROBALL III, A European γ-ray facility, Eds. J. Gerl and R. M. Lieder, GSI 1992.

[27] D. G. Sarantites *et al.*, Nucl. Instrum. Meth. **A381**, 418 (1996).

[28] E. Farnea *et al.*, Nucl. Instrum. Meth. **A400**, 87 (1997).

[29] Ö. Skeppstedt *et al.*, Nucl. Instrum. Meth. **A421**, 87 (1999).

[30] S. Juutinen, J. Hattula, M. Jääskeläinen, A. Virtanen, and T. Lönnroth, Nucl. Phys. **A504**, 205 (1989).

[31] K.S. Krane, R.M. Steffen, and R.M. Wheeler, At. Data Nucl. Data Tables **11**, 351 (1973).

[32] B. Cederwall *et al.*, Nucl. Instrum. Meth. **A354**, 591 (1995).

[33] D. Rudolph, in *Nuclear Structure 98*, Ed. C. Baktash, AIP Conf. Proc. 481, 192 (1999).

[34] M. J. A. de Voigt, J. Dudek, and Z. Szymanski, *High-Spin Phenomena in Atomic Nuclei*, Rev. Mod. Phys. **55**, 953, (1983).

[35] R. Bengtsson and J. D. Garrett, *The Cranking Model-Theoretical and Experimental Basis*, Lund-Mph-84/18.

[36] A.V. Afanasjev, I. Ragnarsson, and P. Ring, Phys. Rev. C**59**, 3166 (1999).

[37] A. V. Afanasjev, J. König, and P. Ring, Nucl. Phys. **A608**, 107 (1996).

[38] G. A. Lalazissis, J. König, and P. Ring, Phys. Rev. C**55**, 540 (1997).

[39] J. Dobaczewski, and J. Dudek, Comp. Phys. Comm. **102**, 166 (1997); **102**, 183 (1997); nucl-th/0003003.

[40] E. Chabanat, P. Bonche, P. Haensel, J. Meyer, and F. Schaeffer, Nucl. Phys. **A635**, 231 (1998).

[41] A. Lopez-Martens *et al.*, in *Nuclear Structure 98*, Ed. C. Baktash, AIP Conf. Proc. 481, 28 (1999).

[42] S. Åberg, Nucl. Phys. **A649**, 392c (1999).

[43] P. Talou, in Proceedings *Pingst2000 - Selected Topics on $N = Z$ Nuclei*, June 2000, Lund, Sweden, Eds. D. Rudolph and M. Hellström, KFS AB Lund, to be published.

[44] C.E. Svensson, in Proceedings of the *International Conference on Achievements and Perspectives in Nuclear Structure*, July 1999, Crete, Greece, Eds. S. Åberg and C. Kalfas, Physica Scripta Vol. T88, 37 (2000).